3

Surface Characterization Techniques

Gökhan Erdoğan, Günnur Güler, Tuğba Kiliç, Duygu O. Kiliç, Beyhan Erdoğan, Zahide Tosun, Hilal D. Kivrak, Uğur Türkan, Fatih Özcan, Mehmet Gürsoy, and Mustafa Karaman

3.1 Introduction

The chemical, physical, and morphological features of surfaces play a very crucial role in material properties including wettability, optical, adhesive, mechanical, and so on. Therefore, diagnosis of surface structures is very important for materials science. The properties of natural and fabricated material surfaces can be determined using characterization techniques. In this chapter, some of the most common characterization methods are given.

3.2 Surface Characterization Methods

3.2.1 X-ray Spectroscopy Techniques

The discovery of X-rays in 1845 by Wilhelm Conrad Rontgen gave rise to significant scientific advancement that benefited a variety of fields by making the invisible to the visible. In 1901, Wilhelm Rontgen received the Nobel Prize in physics for the invention of X-rays. The discovery of X-ray led to significant improvement in the diagnosis for medical applications. In the years subsequent to this discovery, X-rays were used for military applications. Initially, the harmful effects of radiation were not comprehended. Later, it was observed that those who were exposed to X-ray radiation encountered severe burns and skin damages. Thomas Edison's assistant who worked extensively with X-rays, died of skin cancer in 1904. Then, the risk of X-ray radiation was fully understood and this led to the use of protection shields. Today, X-ray technology is being widely employed in numerous fields such as medicine, material analysis, and devices [1].

X-rays are electromagnetic energy waves acting like light rays. X-rays have wavelengths in the angstrom range. Furthermore, X-rays are highly energetic and are employed not only to penetrate solids but also to probe their internal structure. As a result of the atom excitation via high energy photons or electrons, an electron is removed from the atom, leading to an electron hole at the inner orbit. These electron holes are filled by outer electrons. As a result

Surface Treatments for Biological, Chemical and Physical Applications, First Edition.
Edited by Mehmet Gürsoy and Mustafa Karaman.

of this phenomenon, X-rays are produced. The energy released by the excited atom is specific for an element and the intensity related to the amount of the element.

3.2.1.1 X-rays Florescent Spectroscopy

X-ray florescent spectroscopy technique is a powerful and sensitive technique as it allows fast and accurate qualitative as well as quantitative determination of elements. In this technique, the sample is irradiated by the X-rays coming from an X-ray source. X-rays absorbed by the sample are sufficiently energetic to remove electrons located in the inner K and L shell. There are several transitions that yield a fluorescent photon with a characteristic energy equal to the difference in energy of the initial and final orbital as (i) L → K transition is called K_{α}, (ii) M → K transition is called K_{β}, and (iii) M → L transition is called L_{α} [2].

As a result of electron removal, the unstable ions are formed. They become more stable and electron transfer occurs from the outer shells to the inner shells leading to X-ray production. The schematic representation of electron removal from the outer shells to the inner shells is demonstrated in Figure 3.1. This X-ray is called *secondary X-ray*, which is different from the basic X-ray obtained from the X-ray source. The radiation released during the electron transfer from the outer layer to the inner layer is called *fluorescence radiation*. The energy of X-ray fluorescence depends on the energy difference of the electrons transferred between the orbitals.

The intensity of the fluorescent radiation depends on the concentration and the amount of the sample. The fluorescent radiation wavelength can be calculated from Planck's law, given in Eq. (3.1):

$$\lambda = \frac{hc}{E} \tag{3.1}$$

λ is the wavelength
h is the Planck's constant, 6.626×10^{-34} J s
c is the speed of the light, 3.00×10^{8} m s^{-1}
E is the energy.

X-ray florescent spectroscopy (XRF) is one of the most commonly used methods. The samples are not destroyed during the analysis and this method could be

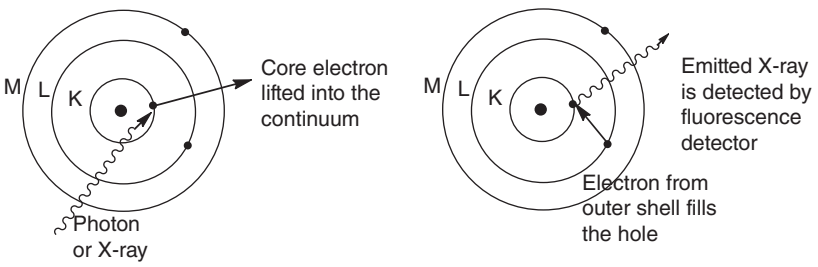

Figure 3.1 The illustration of the electron removal and the X-ray fluorescence radiation.

applied to solids, liquids, and gases. Samples of solid powder are pressed into pellets, liquid specimens are introduced into the cell made from plastic or metal, and gas samples are analyzed at high-pressure vessels. Orbital of transition between the outer and inner layers is between the K and L layers and, conventionally, is often referred to as the transition K_α. The samples are usually in the solid form for XRF applications. Hovewer, the analysis of the solutions can be performed by using appropriate equipments. The solid samples could be transferred on a carriri via pressing a tablet. For the nonhomogenous samples, samples could be melted or dissolved. XRF spectrum is a graphical representation of X-ray intensity peaks as a function of energy peaks. In the spectrum, one can note that the peak energy identifies the element and the peak intensity is indicative of the elemental concentration [3].

3.2.1.2 X-ray Diffraction Technique

X-ray diffraction (XRD) is an analytical technique primarily used for phase identification of a crystalline material. In addition, XRD is employed for monitoring the phase transformation as well as for determining the particle size. It has three basic units: an X-ray tube, a sample holder, and an X-ray detector.

X-rays are produced in a cathode ray tube by heating a filament to produce electrons. The electrons are accelerated through a target by applying a voltage and bombarding the target material with electrons following which a characteristic X-ray spectrum is obtained. In the spectrum there are several components such as K_α and K_β. The commonly used target materials are as follows: Cu, Fe, Mo, Cr. Most researchers prefer the copper target due to its availability with CuK_α radiation (1.5418 Å) [4]. Consider two parallel planes of atoms A–A and B–B in order to understand the diffraction in Figure 3.2. These two planes have the same miller indices h, k, and l. The incoming beam with an angle of θ is monochromatic and coherent. Two rays in this beam, labeled 1 and 2, are scattered by atoms P and Q. Constructive interference of the scattered rays 1 and 2 occurs also at an angle to the planes, if the path length difference between 1-P-1 and 2-Q-2 is equal to a whole number, n, of wavelengths. That is, the condition for diffraction is $n\lambda = SQ + QT$ or $n\lambda = 2d \sin\theta$.

$$n\lambda = 2d \sin\theta \tag{3.2}$$

λ is the wavelength of the X-ray beam
d is the distance between the two lattice
θ is the angle between the incoming X-rays and the normal to the reflecting lattice plane
n is the integer called the *order of reflection*.

The XRD analysis can be done in two different geometries. The first method is generally known as *powder method*, and can be defined as a symmetric method since the system always detects the scattered X-rays at a diffraction angle that is equal to the angle of X-rays incident of the surface. Both the sample and the detector move step by step during the measurement. While the samples rotate at an angle (θ) the detector moves two times this angle (2θ), which is also confirmed in Bragg's law. This method, therefore, always detects the diffracted X-rays

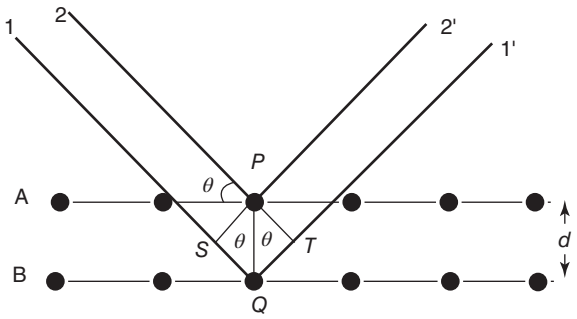

Figure 3.2 X-rays scattered by atoms in an ordered lattice.

from grains that are only oriented parallel to the surfaces and not the others. One disadvantage of this geometry is that the effective depth probed by the incident beam always changes during the scan due to the change in the angle of the incident beam. This property of the method might cause some misinterpretation if it is not taken notice on examining, for example, a material having a layered structure. This introduces the concept of fixing the angle of the incident beam and scanning the scattered beam; for that kind of analysis the following method will be considered.

The second method is used to determine the layered structures. In this system, the incident X-ray beam is fixed to a predetermined value on the sample and detector scans 2θ degrees. Contrary to the powder method, this method facilitates diffraction from the planes not parallel to the surface, never the parallel ones. Normally, this method uses very small angles of incidence on the surface providing information from quite thin layers and is ideally suitable for examination of layer thicknesses, which is on the order of 0.1 μm. The main power behind this method, therefore, involves providing the information layer by layer by just changing the angle of X-ray beam incident on the sample surface. Due to extremely low incident angles the scattered beam mainly lacks enough intensity and parallelism, which might lead to missing or wrong information. Using a Göbel mirror and parallel beam optics may solve this problem. Further information can be found in the literature.

Diffraction patterns are mainly used to identify the crystallographic phases in material characterization. Diffraction peaks are only observed when the sample possesses sufficient long-range order, which is an important limitation. Diffraction lines from perfect crystals are very narrow. The Scherrer equation and XRD spectra was used to calculate the dimensions of the materials. A typical XRD spectra is given in Figure 3.3. Scherrer's equation as follows:

$$\langle L \rangle = \frac{K\lambda}{\beta \cos\theta} \tag{3.3}$$

β is the integral breadth of peak at 2θ values ($\beta = \theta_1 - \theta_2$)
λ is the wavelength of the X-ray beam ($\lambda_{\mathrm{Cu\ K_\alpha}} = 1.54\,\mathrm{nm}$)
θ is one half of the deviation of the diffracted beam and the normal reflecting line
L is the interplanar spacing for a plane.

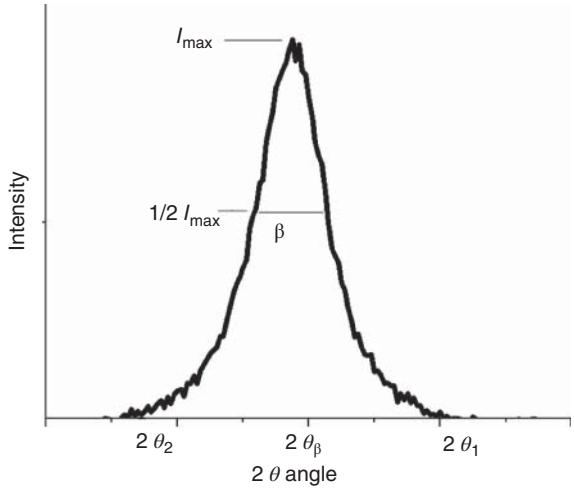

Figure 3.3 X-ray diffraction pattern.

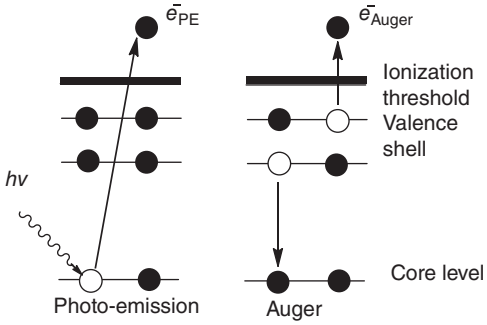

Figure 3.4 Auger processes and X-ray process.

3.2.1.3 X-ray Photoelectron Spectroscopy

X-ray photoelectron spectroscopy (XPS) provides information on the elemental composition and the oxidation state of the elements. Photoelectric effect is crucial for the XPS theory. Mg K_α (1253.6 eV) and Al K_α (1486.3 eV) are the most commonly used X-ray sources. In XPS, one measures the intensity of photoelectrons as a function of their kinetic energy.

The sample is irradiated with a monochromatic X-ray beam. An ejected photoelectron leaves behind a core hole in the atom. The hole created in the shell gives rise to a photoelectron. This hole if filled by an electronic transition from the other shell. The energy released is associated with the X-ray photon (see Figure 3.4). Each atom has core level electrons. The binding energy of each core level electron is specific. The measured kinetic energy of a core level photoelectron peak can be related directly to its characteristic binding energy. The energy of core level electrons depends on the chemical state of the atom. Binding energies on the XPS spectrum are not only element specific but also contain chemical information. As a rule of thumb, the binding energy increases with the oxidation state or with the electro negativity of its neighbors [4, 5].

Photoelectron peaks are labeled according to the electron quantum numbers. An electron has an orbital momentum l (0, 1, 2, 3… Indicated as s, p, d, f…) and

a spin momentum. The total momentum of this electron could be predicted as $j = l + s$. Each level has two levels as the spin may be either up ($s = +1/2$) or down ($s = -1/2$). The energy difference is called the *spin orbit splitting*.

3.2.2 Surface Characterization with FTIR Spectroscopy

Fourier transform infrared (FTIR) spectroscopy is a kind of molecular vibrational spectroscopy that provides information about the chemical composition, bonding properties, and atomic and molecular structure (and environment) of materials at the molecular scale. FTIR spectroscopy has been extensively used as a surface characterization, analytical, or biophysical technique for the study of a variety of materials including chemical and biological species as well as drugs, thin films, coatings, synthetic polymers, natural biopolymers (DNA, protein, etc.), biomaterials, nanoparticles, and biomedical samples (dental implants etc.) [6–12]. FTIR technique enables to measure all type of materials (solids, liquids, and gases).

Infrared (IR) spectroscopy is based on the interaction of IR radiation with an oscillating electric dipole moment of the molecules. The IR region covers the range of 0.7–500 μm (14 000–20 cm^{-1}) and is divided into three parts as being near-IR (0.78–2.5 μm), mid-IR (2.5–50 μm), and far-IR (50–500 μm) radiation. The mid-IR range (4000–400 cm^{-1}) is the most useful region of the electromagnetic spectrum for the analysis of biological macromolecules, chemicals, and polymeric materials.

Atoms and molecules interact with electromagnetic radiation in a wide variety of ways (absorbing and/or emitting). Absorption of electromagnetic radiation stimulates different types of motion in atoms and/or molecules. For example, absorption of the IR radiation by the sample excites the interatomic vibrations (or normal modes). These normal modes are described by stretching (symmetric and antisymmetric), bending, rocking vibrations, and so on. If the frequency of IR light coincides with the frequency of molecular vibration and if stretching of bonds between the atoms creates a dipole moment change along with the vibration (IR-active), then the incident IR beam is absorbed by a molecular vibration of the sample, generating an IR spectrum (Figure 3.5). The pattern of absorption is called *spectrum (sing.) or spectra (pl.)*. The amount of IR light (or intensity)

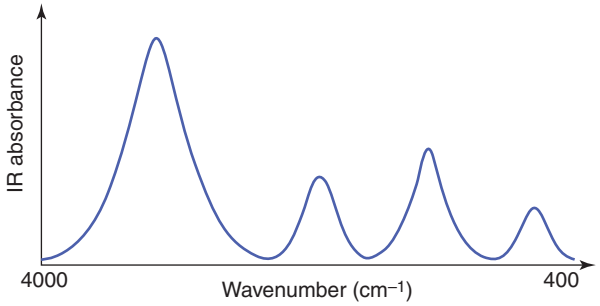

Figure 3.5 A schematic representation of an FTIR spectrum. (Image Courtesy of Günnur Güler.)

absorbed by the material is plotted as a function of wavenumber. Wavenumber is the number of waves in a space and is depicted by the reciprocal of wavelength. Wavenumber (cm^{-1}) is used as the unit of energy in a spectrum since it is proportional to the frequency and energy due to

$$\text{wavenumber} = \frac{1}{\lambda} = \frac{\vartheta}{c} \tag{3.4}$$

$$\text{energy} = h\vartheta \tag{3.5}$$

where h is the Planck constant, ϑ is the frequency, and c is the speed of light. Vibrational modes that do not generate a dipole moment change in the molecule are called *IR-inactive* (not observed in the IR spectrum) such as symmetric stretching modes of CO_2 and homonuclear diatomic molecules (H_2, N_2, and O_2) while heteronuclear diatomic molecules (CO and HCl) are IR active having induced dipole moment due to the change in the atomic positions (dipole moment = charge × distance).

FTIR technique is used to determine the presence of the functional groups (i.e., OH, NH, CH, CO, and PO) in materials. The IR radiation absorbed by the vibrations of functional groups gives rise to the characteristic IR signals at specific wavenumbers (or frequencies). These signals are unique for a given compound and the absorbed intensity is associated with the quantity of the absorber. Atoms within a molecule oscillate with a frequency of

$$\vartheta_{\text{vib}} = \frac{1}{2\pi}\sqrt{\frac{k}{\mu}} \tag{3.6}$$

where μ is the reduced mass of the atoms and k is the force constant of the bond between molecules or atoms. Different vibrational modes are detected at different frequencies in the spectrum because a characteristic frequency depends on two important parameters. These are the masses of atoms and the bond length between atoms. This makes IR spectroscopy very sensitive to any changes in the molecular environment. Frequency decreases with increasing atomic mass while it increases with increasing bond energy (k). Therefore, an IR spectrum provides a fingerprint pattern of molecular structure of the material, which is composed of thousands of atoms.

3.2.2.1 FTIR Spectrometers

An FTIR spectrometer is an instrument that displays the IR spectrum of a sample. In the 1940s, the dispersive IR spectrometers were developed with a grating monochromator used as an analytical technique for the characterization of compounds. However, modern FTIR spectrometers have been used for advanced researches since the late 1970s, which use a Michelson interferometer to record an IR spectrum.

A Michelson interferometer is the most important component of the spectrometer [13, 14]. It harbors a source, beam splitter, two plane mirrors (one fixed and one movable), a laser, and a detector. The collimated IR beam, which passes through the interferometer, is split into two beams via the beam splitter. After recombination, a constructive or destructive interference pattern is created and is directed to the output. The output IR beam passes through the sample

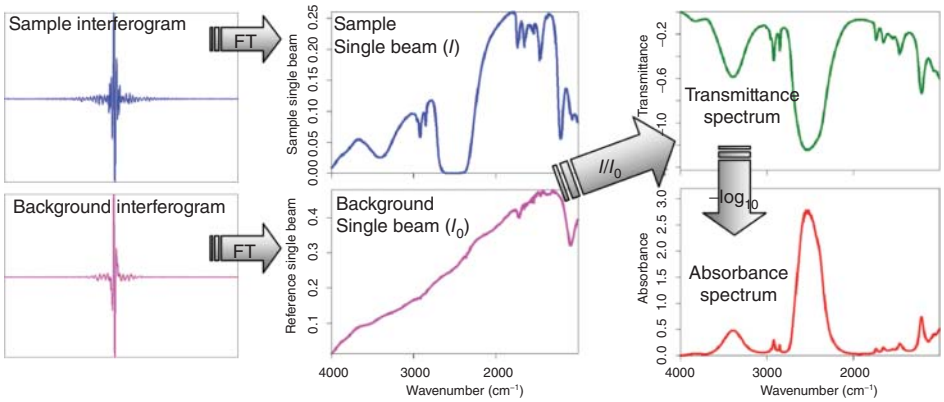

Figure 3.6 The process of formation of a Fourier transform (FT) infrared spectrum drawn by OPUS software [15]. (Image Courtesy of Günnur Güler.)

where some energy is absorbed and some is transmitted. The transmitted light is focused toward the detector. The optical path length of a beam varies with a movable mirror. The detector signal (output) is collected as an interferogram (Figure 3.6). This interferogram is transformed to the frequency domain by a computer using the mathematical operation called Fourier-transformation at discrete points to display the IR single beam spectrum. To produce *absorbance or transmittance spectrum*, the *sample single beam spectrum* is collected taking the reference as *background single beam spectrum* (Figure 3.6). This reference spectrum is recorded in the absence of a sample; for example, the air spectrum. The final spectrum (i.e., transmittance spectrum) can be converted to one another (i.e., absorbance spectrum) by calculating the negative logarithm ($A = -\log_{10} T$) of the data points. The absorbed IR radiation (A) by a sample can be directly calculated by *Beer-Lambert law:*

$$A = -\log_{10}\left(\frac{I}{I_0}\right) \tag{3.7}$$

where (I) and (I_0) are the intensities of the single beam spectrum of the sample and reference, respectively.

For FTIR spectrometers, photon detectors (semiconductor detectors such as mercury-cadmium-tellurium or MCT) and thermal detectors (deuterated triglycine sulfate or DTGS) are available to measure the intensity of the incident beam. MCT detectors operate at liquid nitrogen temperature of about 77 K while DTGS detectors work at room temperature.

3.2.2.2 Methods and Sampling Techniques

An IR spectrum can be recorded by FTIR spectrometers combined with attenuated total reflection unit-Fourier transform infrared (ATR-FTIR) or in the transmission mode. Both are absorption techniques. FTIR can identify even small concentrations of materials (typically 0.1 – 1 mM).

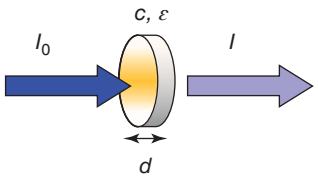

Figure 3.7 A schematic representation of an absorption measurement with FTIR in the transmission mode [15]. (Image Courtesy of Günnur Güler.)

FTIR in transmission mode: In transmission measurements, the IR beam is passed through a cuvette before it reaches the detector (Figure 3.7)

$$A = \varepsilon cd = -\log_{10}\left(\frac{I}{I_0}\right) \tag{3.8}$$

The absorbance is calculated from the Beer-Lambert's law, where c is the concentration of the absorbing molecules, ε is the molar extinction coefficient (or molar absorption index), and d is the path length of the measuring cuvette. Thus, this technique is suitable for quantitative analysis. Importantly, the FTIR cuvettes (or optical materials) should be transparent in the mid-IR spectral range so that only IR signals arising from the measuring sample are observed in the spectrum. Such optical materials can be ZnSe, AgCl, KRS-5, KBr, CsBr, CsI, KCl, NaCl, CaF_2, and BaF_2 that have different stability against aqueous solution and different refractive indices. A suitable path length has to be selected for liquid samples. For example, CaF_2 is the most widely used cuvette to study aqueous solutions of materials due to its insolubility in water and low refractive index.

In comparison to aqueous solutions, analyzing of solid samples is rather complex for a transmission measurement. A certain amount of solid sample must be diluted with KBr that is transparent in the IR range. Subsequently, the mixture of KBr and the solid sample is pressed to make "KBr-pellet." Homogenization of this pellet is crucial to obtain a high quality and reproducible spectra. Therefore, ATR-FTIR spectroscopy is mostly preferred to get rid of preparing of KBr-pellets.

ATR-FTIR spectroscopy: One of the most frequently applied experimental methods for surface characterization is the ATR-FTIR spectroscopy. It is an absorption technique that soft materials (biological and chemical species, polymers, gels, pastes, semi-dry films, 2D crystals, and proteoliposomes of protein–membrane complexes) as well as hard materials (thin films, powders, metals, etc.) can be easily analyzed without particular sample preparation.

The IR beam is directed to a trapezoidal-shaped IR-transparent crystal with a high refractive index, n (Figure 3.8). The crystal material is mostly capped with zinc selenide ($n = 2.42$), diamond ($n = 2.4$), or germanium ($n = 4$), where the sample material is placed (Figures 3.8 and 3.9). The incident light is reflected at the interface between two materials. which is made up of different refractive indexes. The reflected IR beam is attenuated and protrudes a few micrometers (0.5–5 μm) into the sample medium ($n_{sample} = \sim 1.5$). IR radiation is partially absorbed by the sample deposited on the surface of crystal plate. Therefore, ATR-FTIR is a kind of surface sensitive technique and sometimes also stands for evanescent wave spectroscopy. It is easy to use because the material is just placed on the top of the ATR unit. Solid materials such as thin films, coatings, powders, metals, papers, rubber, fibers, leather-like samples, and polymers can pressed with a pressure tip

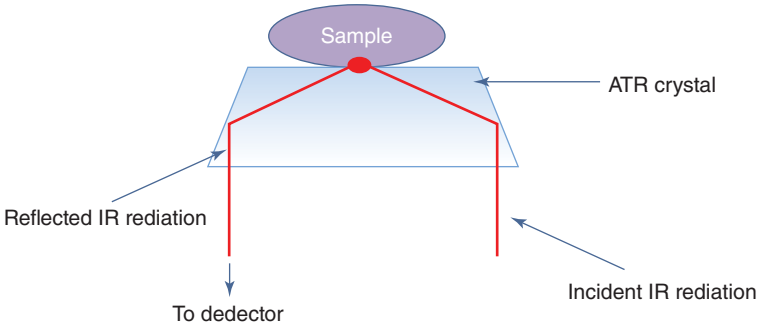

Figure 3.8 A schematic representation of an ATR unit. IR beam undergoes internal one-single reflection in the ATR crystal of high refractive index. The sample is in contact with the crystal. (Image Courtesy of Günnur Güler.)

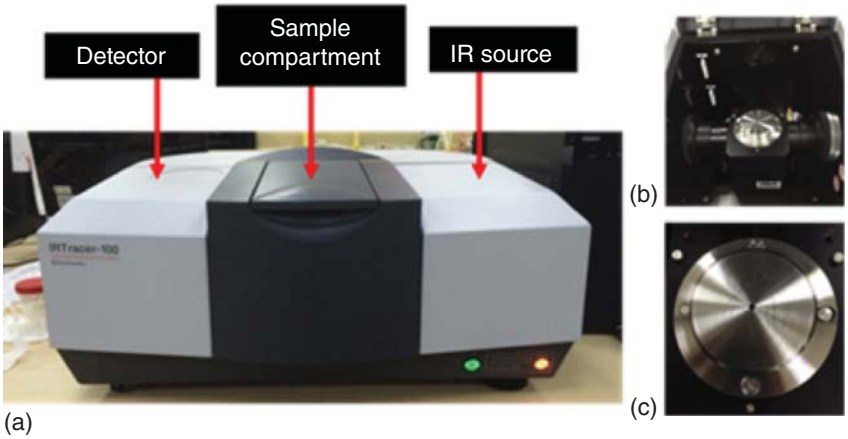

Figure 3.9 The FTIR spectrometer (a) equipped with an ATR unit and crystal plate (b). Image at (c) shows the sampling area made up of diamond. (Image Courtesy of Günnur Güler.)

of a high-pressure clamp to provide an intimate physical contact with the crystal plate. This technique requires only a tiny amount of sample but should be in good contact with the sampling area to produce a strong and reproducible IR signal. Therefore, it is well suited particularly for the surface characterization of the materials.

3.2.2.3 Advantages and Disadvantages of FTIR Spectroscopy

In comparison to other techniques, FTIR spectroscopy has many advantages. FTIR spectrometers provide high spectral accuracy with high signal-to-noise ratio, high resolution, and sensitivity to weak peaks. The technique is also economic, nondestructive, and fast. It is easy to use and one spectrum is measured very quickly within seconds or a couple of minutes. It does not change the structure of the samples due to small photon energy (0.05–0.5 eV). FTIR requires a small amount of sample; particularly, a few microliters (or one drop) of liquids and one pinch of solid material are enough for the FTIR measurements.

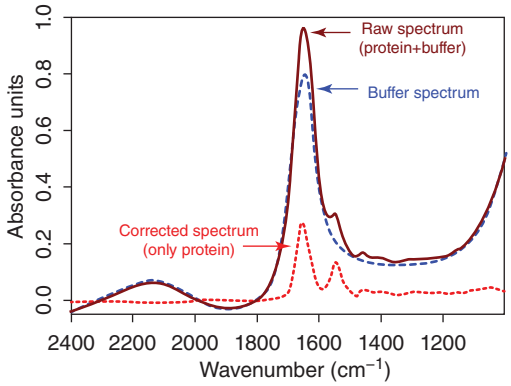

Figure 3.10 The FTIR absorbance spectra of the osmosensor protein BetP in *aqueous solutions* before (raw spectrum) and after (corrected spectrum) H_2O buffer subtraction [15]. (Image Courtesy of Günnur Güler.)

However, FTIR spectroscopy has some limitations. Particularly, studying with aqueous solutions has certain difficulties because water has an intense absorbance due to O—H vibrational signals that overlap strongly with the signals of other functional groups. This problem can be overcome by taking the water as a background before measurement of the real sample or the spectrum of the water/buffer solution can be mathematically subtracted/corrected from the real sample spectrum (see Figure 3.10) so that we can get rid of the water absorption in the spectrum. The other disadvantage is that FTIR provides only average information from one type of functional group. For example, the C=O vibrational modes of two different types of materials are observed at the same frequency range with a minimal frequency shifting depending on the local and global environment of the C=O molecules.

3.2.2.4 Applications of FTIR Spectroscopy

IR spectroscopy is one of the classical methods used as a characterization technique to explore chemical bonds in surface atoms in many research areas, including organic and inorganic chemistry, solid state physics, material science, biotechnology, biomedical engineering, biophysics, biochemistry, and pharmacy.

FTIR is a time-saving and nondestructive technique that requires low set up and running cost. Importantly, it provides label-free analysis of materials. This makes FTIR spectroscopy a valuable tool for the characterization of structural and physicochemical properties of materials such as dynamics and flexibility, stability, purity, ionization (protonation or deprotonation), thermodynamics, binding, kinetics of a reaction, structure determination, identification of chemical and molecular composition, surface modifications, and structural inhomogeneity. FTIR is also sensitive to single bonding changes, thus, FTIR technique can determine with great confidence the bond length, bond strength, H-bonding properties, conformational freedom, charge distributions, redox state, and electrostatic interactions in a material.

Surface characterization studies using FTIR spectroscopy for chemical analysis have been performed on a variety of nanoparticles that show potential for drug delivery systems [6, 7]. For instance, zein–pectin capsule was developed for target delivery [6]. Here, the ATR technique was used to analyze the characteristic chemical interactions between pectin (a carbohydrate) and zein (a protein) which

are the natural biopolymers. Formation of the zein – pectin complex via hydrogen bonding was confirmed in the IR spectra.

FTIR spectroscopy has been primarily used for surface chemistry of nanostructures and nanoparticles as well [16, 17]. For example, different types of nanostructures (nanobelts, nanobricks, and nanosheets) of polypyrrole (PPy), which are very promising polymers for the electrochemical supercapacitors, were fabricated [16]. Polymerization of pyrrole was achieved electrochemically. Subsequently, they were analyzed with FTIR spectroscopy to confirm the formation of conducting PPy thin films. Observation of characteristic IR signals absorbing at 1194 cm^{-1} (C—N stretching vibrations) and 922 cm^{-1} (C=C in-plane bending vibrations of the pyrrole ring) reflect the doping state of PPy thin film. ATR-FTIR spectroscopy is a powerful tool for the surface characterization of polymeric materials. It provides surface-specific information since the penetration depth of the IR beam can protrude deeply into the surface of a material. For example, polymers of HEMA (2-hydroxyethyl methacrylate) are used in many biomedical applications like drug delivery and biosensors. Thin films of poly-HEMA at various conditions have been extensively analyzed with FTIR technique [18].

FTIR is particularly well suited for the analysis of polymer processing (surface modifications, coatings, etc.). Surface modifications of commercial ultrafiltration polyethersulfone membranes achieved by a graft polymerization technique were characterized by the ATR technique to reveal the chemical changes during modification [12]. In this work, FTIR could also recognize the adsorption of the albumin protein on the surface of these membranes. It was also able to detect the conformational changes of the albumin during adsorption. Thus, the ATR technique is very useful for binding or adsorption studies [19] with biological systems such as proteins, nucleic acids lipids, and so on. Since ATR is a surface-sensitive technique, conformation analysis of adsorbed proteins, orientation of molecules/functional groups, surfactants, and drugs can be studied well.

When compared to other techniques, FTIR spectroscopy is highly effective for surface characterization. It has been commonly used also for the characterization of thin films, nanowires, and coatings in terms of molecular ordering/disordering, bonding arrangements, trace impurities as well as associated chemical imperfections. For example, SiO_2 or silica-like thin films and nanowires deposited directly on the ATR crystal have been studied for many years [20–23]. In these studies, the Si—O—Si bonding vibrations (—O—Si—O—) detected in the IR range of 1000–1250 cm^{-1} are related to interface roughness and structural disordering. Particularly, a major absorption band centered around 1070 cm^{-1} refers to the structural disordering. An increment of the intensity of this band was correlated with the structurally disordered amorphous SiO_2.

FTIR spectroscopy has been also used in the field of material science and solid state physics to investigate the dynamics of atoms in crystals due to phonons [24–27]. Normal modes in molecules and phonons in crystals are the detected vibrational modes of materials. IR spectra of rock minerals such as calcite ($CaCO_3$), which has a trigonal structure with two molecules per unit cell as well as dolomite ($CaMg(CO_3)_2$) which has a hexagonal structure, have been

analyzed [24]. Since their structures are very similar, their IR spectra resemble, but FTIR spectroscopy can distinguish these crystals by following the spectral shifts in wavenumbers. Other crystal lattices such as $(GaAS)_n/(AlAs)_m$ [26, 27] and InAsSb/GaSb superlattices [28] have been also characterized with FTIR spectroscopy.

Characterization of the surface modifications and biochemical properties of the implants (bone and dental implants, etc.) and biomaterials (calcium hydroxyapatite, etc.) are crucial for their interactions with the surrounding tissue/cell since it affects the bioactivity and biocompatibility. Thus, FTIR spectroscopic characterization has become increasingly valuable in the biomedical field [29–31]. Titanium-based implants and Ca^{2+}-alginate hydrogel implants are some examples analyzed with FTIR spectroscopy. Dental implants coating with hydroxyapatite using two different processes (plasma spray and modified biomimetic process) was also characterized with FTIR [8].

FTIR technique is frequently used for analyzing of tissue, cell, and biological macromolecules like peptides, proteins, lipids, carbohydrates, and nucleic acids (DNA, RNA, and microRNA), and even individual amino acids. For example, molecular and biochemical characterization of cells [9] and tissues [13, 30], 2D crystals and proteoliposomes of protein–membrane complexes [10, 15], analysis of secondary structure of proteins and characterization of enzyme–substrate reactions [14, 32–34], lipid–protein interactions [10, 35], and nucleic acid–drug interactions [36–38] are some examples studied by FTIR spectroscopy. These studies provide information on biochemical and biophysical characteristics, such as determination of conformational changes and functional features of proteins, inter- and intra-molecular interactions with their environment, bonding arrangements, dynamics and flexibility of molecules, stability, protonation–deprotonation status.

3.2.3 Nuclear Magnetic Resonance Spectroscopy

Nuclear magnetic resonance spectroscopy (NMR spectroscopy), is a nondestructive analytical technique that determines the unique structure and also enables conformational analysis of a compound by exploiting the magnetic properties of certain atomic nuclei. The technique has been discovered simultaneously by two research groups Edward M. Purcell, Howard C. Torrey, Richard V. Pound from Harvard University and Felex Bloch, William W. Hansen, and Martin Packard from Stanford University upon observing the phenomenon of NMR in both solids and liquids [39]. NMR spectroscopy has been applied to a wide range of disciplines including chemical sciences, biological and biochemical research, food industry, pharmaceutical development and production, polymer industry, and even geophysics. It has also led to the development of magnetic resonance imaging (MRI), which uses the same principle as NMR to get an image of a soft tissue [40, 41].

As one of the surface characterization techniques, NMR spectroscopy has been widely used for the characterization of solid materials both in bulk and surface structure. It has also been implemented to understand the surface reactivity, oxidation state, and structure of active species as a complementary

technique to other alternative methods like XRD and high-resolution electron microscopy [42].

3.2.3.1 Theory of NMR Spectroscopy

Subatomic particles included in a nuclei are considered as spinning on their own axes. However, in many atoms (like ^{12}C) that have even number of protons and neutrons, these spins are paired and the overall spin, I, of the nucleus becomes zero (so called NMR inactive). Otherwise, the atomic nucleus has an overall spin; when both the numbers of neutrons and protons are odd numbers, it will be an integer (1, 2, 3, etc.); on the other hand, if the sum of the number of protons and number of neutrons is odd, it will be a half-integer (1/2, 3/2, etc.). The overall spin generates a randomly oriented magnetic field. When an external magnetic field B_0 is applied, two spin states exist: +1/2 (lower energy level) and −1/2 (higher energy level) and the nuclear magnetic field align itself either with or oppose the external magnetic field due to absorption and re-emission of electromagnetic radio frequency radiation (roughly 4–900 MHz). When the spin of the nuclei flipped, the nuclei are said to be in resonance with B_0. The frequency at which the *resonance* occurs is called *Larmor frequency* measured in an NMR experiment and is a unique property of a nucleus since every nucleus absorbs electromagnetic radiation at different wavelengths/frequencies (Figure 3.11).

Additionally, every specific nuclei enters resonance at different energies and frequencies depending on their chemical and electronic environment. Since charged particles surround the nucleus by moving in a loop to create a magnetic field, the "experienced" magnetic field by the nucleus is slightly different from the external magnetic field applied. This phenomenon is called *nuclear shielding* and the resultant change in energy levels requires a different frequency for resonance which in return results in a new peak in an *NMR spectrum*. The basis of structural and conformational analysis of molecules relies on nuclear shielding and *chemical shift* (δ) which is a term used to describe the relative resonance frequency of a certain compound to a reference compound and represented by the formula:

$$\delta = \frac{\upsilon_{sam} - \upsilon_{ref}}{\upsilon_{ref}} \tag{3.9}$$

where υ_{sam} is the absolute resonance frequency of a certain sample while υ_{ref} is an absolute resonance frequency for a standard compound under the same external

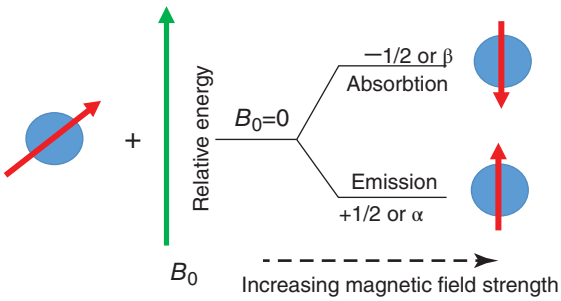

Figure 3.11 Energy levels of a nucleus with $I = ½$ after an exertion of a magnetic field B_0.

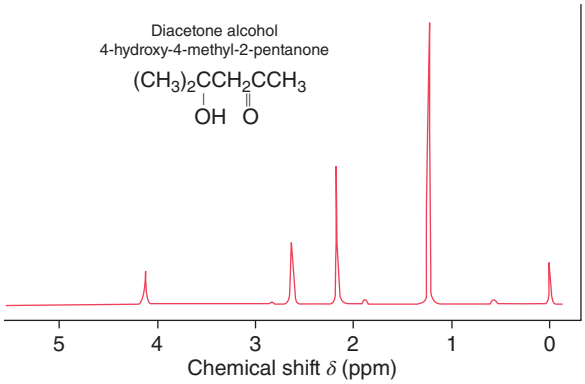

Figure 3.12 Sketch of a proton NMR spectrum included in Becker, Chapter 1.

magnetic field. As a standard compound, generally tetramethylsilane (TMS) has been used.

In an NMR spectrum that consists of a set of peaks as exemplified below, each peak corresponds to a distinct compound. The *x*-axis shows the frequency in parts per million and the *y*-axis shows the absorption peaks (Figure 3.12).

3.2.3.2 Types of NMR Spectroscopy

There are various types of NMR spectroscopy depending on:

- The type of instrumentation used
  - *Continuous wave NMR*: The absorbance of the sample under resonance is recorded as a function of either radio frequency (RF) excitation or magnetic field. In continuous-wave (CW) NMR, both RF excitation and magnetic field are continuously on.
  - *Fourier transform NMR*: The sample of interest is irradiated with a specific range of frequencies for a specific time and the decay of signal over time (FID; free induction decay) is observed till the relaxation (return back to the ground state energy level) and then converted to signal-frequency domain.
- The type of nucleus involved
  - *Carbon-13 NMR*: used for identification of carbon atoms, only ^{13}C isotope that accounts for 1% of all organic molecules since ^{12}C is not NMR active, in a substance and has a wide variety of use in organic chemistry for structure elucidation.
  - *^{1}H NMR*: Also known as *proton NMR* used to identify the structure of a compound with respect to hydrogen by providing information regarding the number of different H present in a molecule, the electronic environment of the different types of hydrogens, the number of hydrogen neighboring a hydrogen. For solution-based measurements, inert solvents that do not contain protons (deuterated, ^{2}H = Deuterium/D) like; D_2O (deuterated water), $CDCl_3$ (deuterated chloroform) are used.
- The physical state of the sample
  - *Solid state NMR*: NMR conducted in solids. The NMR spectra seems to be broadened due to dipolar interactions and chemical shift anisotropy (orientation dependence of the chemical shift). For high resolution solid state

NMR, various methods have been used: magic angle spinning, dilution, multiple pulse sequences, cross-polarization [43].
  - *Solution state NMR*: most of the NMR experiments are done in solution phase due to rapid molecular motion of solutions.
  - *Gas state NMR*: used to expand the molecular electronic properties, to yield temperature-dependent experimental data and observe intermolecular effects on molecular electronic properties [44].
- The data collection
  - *One dimensional NMR* (i.e., Carbon-13 NMR, ^{1}H NMR): only x axis has a chemical shift scale, y axis shows the intensity.
  - *Two-dimensional NMR* (i.e., homonuclear 2D, heteronuclear 2D): both the x and y axes have chemical shift scales and the data is collected in 2D as a grid-like map. The structural determination is done by looking at the spectra at the peaks in the grid and by matching them to the *x* and *y* axes. Intensities used as third axis. There are several types of 2-D NMR; COSY (correlation spectroscopy, both axes corresponds to ^{1}H NMR), HETCOR (heteronuclear correlation spectroscopy where ^{1}H NMR and ^{13}C NMR are used in *x*- and *y*-axis).

3.2.3.3 Instrumentation and Sample Handling

A typical NMR instrument basically consists of four main components: a magnet, a frequency generator, a detector, and a recorder as illustrated in Figure 3.13. The magnets used in NMR instruments are superconducting responsible for providing a homogeneous magnetic field at 60–100 MHz. The induction of the magnetic field is provided by magnetic coils when alternating current created by frequency generator flows through them. The frequency generator could work either as a continuous wave or pulsed. The detector subtracts the base frequency

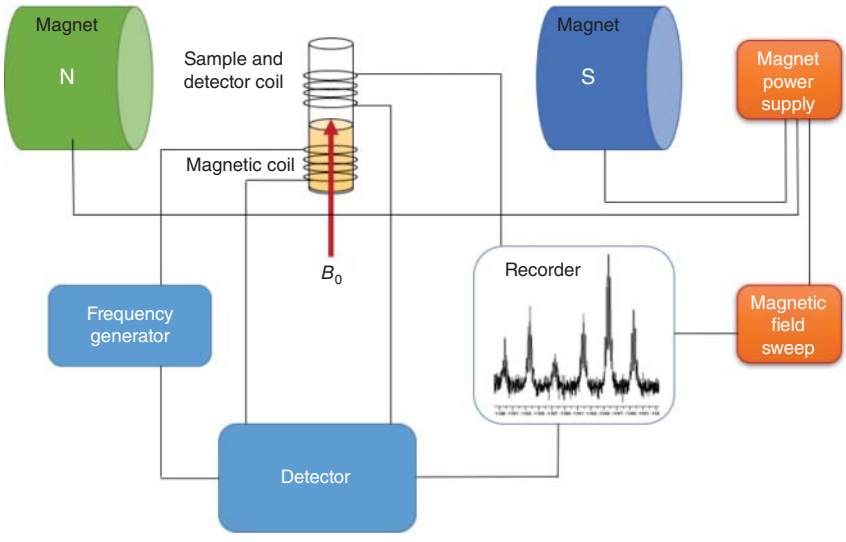

Figure 3.13 Typical sketch of an NMR instrument.

from the output frequency and recorder can be of in various types: oscilloscopes, computer, and so on.

3.2.3.4 Applications of NMR

NMR has become an indispensable tool for analytical technology and has taken a pivotal role in a wide variety of applications in many disciplines. Not only scientific disciplines but also various industries take advantage of sophisticated NMR for routine analysis and basic research. Some examples have been given below to give insight about the usage of NMR. For detailed explanations and other examples other reference books and reviews dedicated for this aim could be followed [40, 45–50].

Biochemistry: to analyze the biomacromolecules up to 100 kDa for structure determination, to identify the protein function and protein folding, to do atomic resolution structure analysis on membrane or such environments, motional properties of biomacromolecules, determination of ionization state of the enzymes, determination of interior water of proteins, and analysis of hydrogen bonding for several biomolecule interactions.

Pharmaceutical: drug screening, drug design, drug–protein drug/enzyme interactions, and drug–receptor interactions.

Chemistry: structural elucidation and conformational analysis of compounds.

Material science: polymer chemistry, physics, silicates (i.e., minerals, zeolites).

Food analysis: determination of oil content of a product (seeds, meals, and meat, etc.) and determination of humidity in various foodstuffs.

3.2.4 Electron Microscopes

An electron microscope uses electrons to form a magnified image. This magnified image is the ratio of the image size on the screen to the size of the object that is being examined under a microscope. To understand why it is essential to use electrons instead of light for high magnified images we need to know the definition of resolution and depth of field.

Resolution is the minimum distance that a microscope can resolve. Resolution of an optical microscope is limited due to the nature of visible light. The wavelength of visible light is between 400 and 700 nm. The electron energy in an electron microscope can change from 0.1 up to 300 keV. The wavelength changes with the energy and, therefore, the wavelength is not constant in a whole electron energy range

$$E = hc/\lambda \tag{3.10}$$

For 10 keV of electron energy wavelength of an electron based on Eq. (3.10) is 0.12 nm. When the wavelength of visible light is compared with the wavelength of an electron it is seen that the resolution of an electron microscope is more powerful than that of an optical microscope.

The depth of a field is related to the features in the image. It is a measure of how many of these features are in focus at the same time. Electron microscopes have higher depths of field when compared to light microscopes.

Electron microscopes not only give information about topography and morphology but also of composition and structure. These are the information that a light microscope cannot supply.

There are two types of electron microscopes, scanning electron microscope (SEM) and transmission electron microscope (TEM). We will now investigate them in detail.

3.2.4.1 Scanning Electron Microscope (SEM)

SEM is generally preferred for a wide range of applications such as metals, polymers, ceramics, and surface coatings due to its wide range of capabilities such as getting high resolution and three-dimensional images and compositional, topographical, and morphological information about any solid materials.

The first SEM idea was proposed by Knoll in 1935. It was far beyond being a SEM but Von Ardenne in 1938 built a scanning transmission electron microscope (STEM) by adding a scanning coil to a TEM. STEM mode is still a standard imaging technique in modern microscopes. In 1942, Zworykin made some improvements in SEM design. Oatley from Cambridge University built a microscope with a better resolution in 1948 and, in 1965, the first commercial SEM was built by Cambridge instruments [51].

SEM, as it is in the other types of electron microscope, uses a focused beam of electrons that are produced in the electron source at the top of the microscope. The electron source has an area and this area is dependent on the type of the source that is being used. There are three types of electron sources: thermionic sources, Schottky emission sources, and field emission sources. Sources have an effect on the resolution and the best resolution is achieved in field emission electron sources. The electron beam follows a vertical path due to electromagnetic lenses through the column of the microscope. Electromagnetic lenses focus and direct the beam down to the sample. When the beam hits the sample the electrons interact with the specimen. The interaction is directly proportional to the energy of incident beam. This is called *interaction volume* and it becomes broader when the energy is increased. The electrons do not follow a straight line in the sample as it is seen in Figure 3.14. They follow a zig–zag path instead.

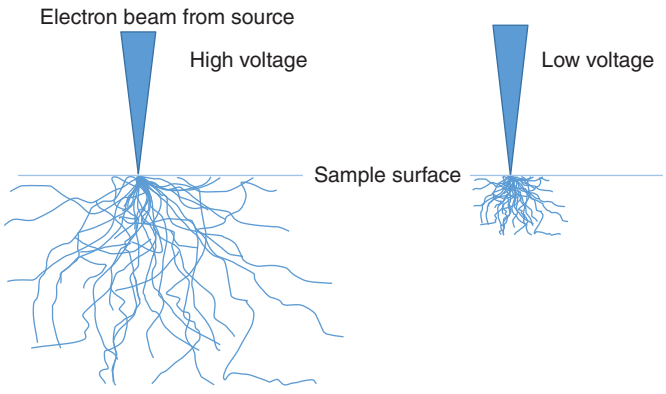

Figure 3.14 Interaction volume for high and low voltage.

Following this interaction a variety of characteristic signals are generated and every signal is detected by its own detector. Secondary electrons are detected by Secondary Electron (SE) detector, Back scattered electrons are detected by Back Scattered Electron (BSE) detector, X-rays are detected by Energy Dispersive X-ray Spectroscopy (EDS) detector and Transmitted electrons are detected by Scanning Transmission Electron Microscopy (STEM) detector as it is seen in Figure 3.15.

Characteristic signals after being detected by specific detectors are converted to a signal on the screen as an image. In Figure 3.16, an SE image of ZnO crystals is seen. This image is acquired using SE detector and it shows the topography of the ZnO crystals.

In Figure 3.17, a BSE image of gold particles on textile fibers using BSE detector is shown. This detector uses atomic contrast. A brighter BSE intensity correlates with higher average atomic number. The brighter the region of interest, the higher the atomic number and the darker the region of interest the lower the atomic number is.

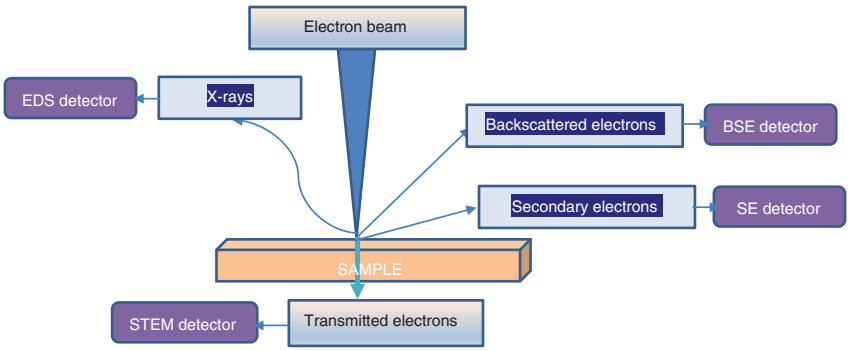

Figure 3.15 Electron beam and sample interaction.

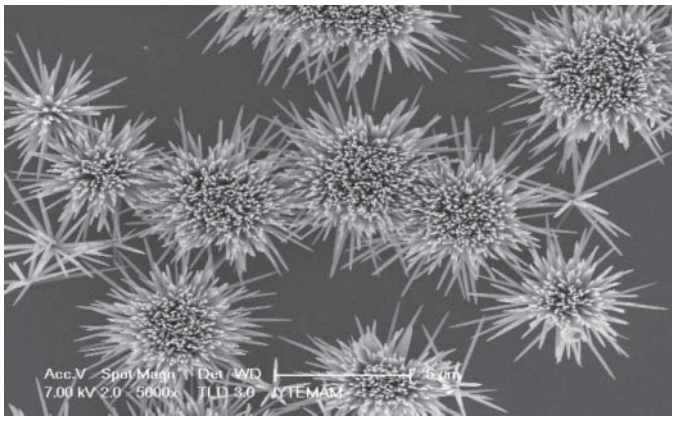

Figure 3.16 ZnO crystals.

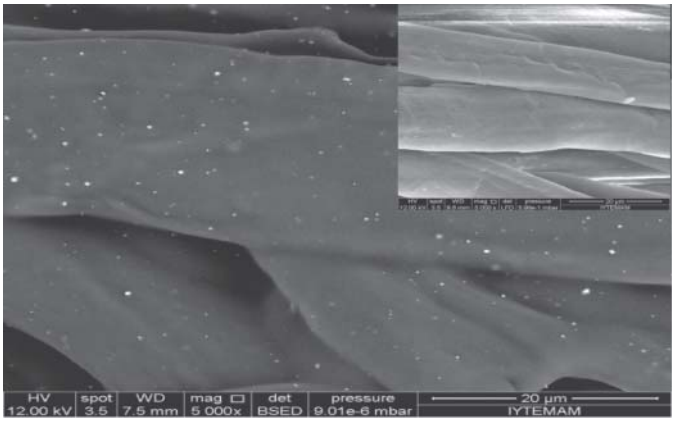

Figure 3.17 BSE image of gold particles.

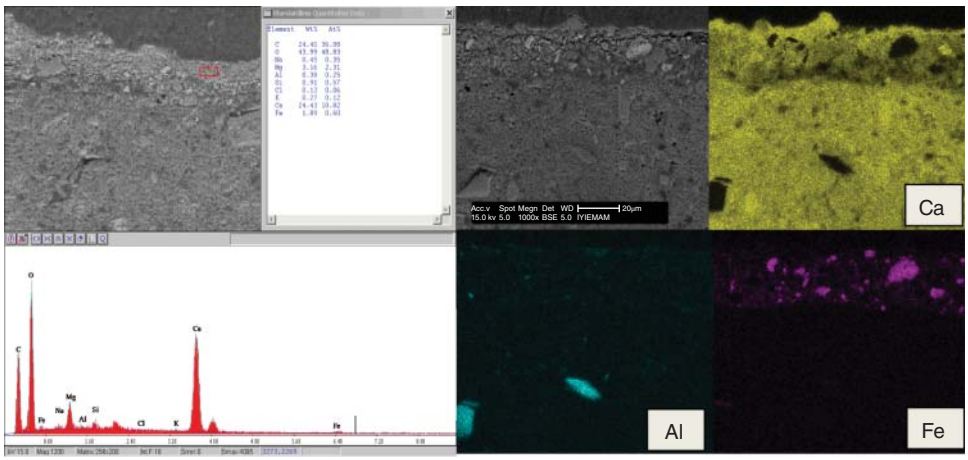

Figure 3.18 EDS image and elemental mapping of a ceramic sample.

Using X-ray imaging techniques one can get information about the composition of the sample by examining the qualitative and quantitative analysis and the elemental mapping of the sample. In Figure 3.18, a quantitative analysis of a ceramic material and its elemental mapping are seen.

Using a very thin sample, prepared by TEM sample preparation methods that will be described in Section 3.2.4.3, electrons pass through the sample and these transmitted electrons are observed using a STEM detector. In Figure 3.19a, a STEM image of gold particles on polystyrene latex is seen.

The detectors used to acquire the images discussed above are seen in Figure 3.20.

Sample Preparation for SEM Samples examined under SEM must be conductive, humid, and oil free. If the sample to be examined is not conductive, a sample coating procedure must be followed. One of the sample coating procedures for a SEM sample preparation is sputter coater. In this coating system Ar gas is used

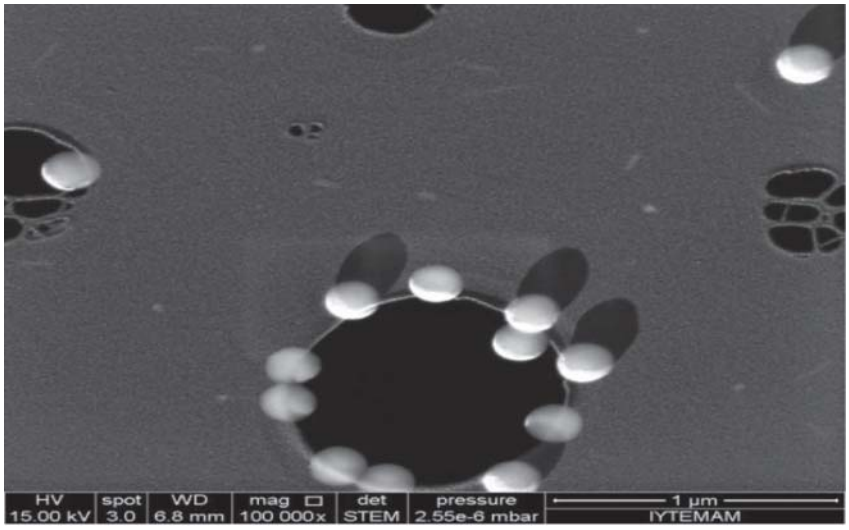

Figure 3.19 STEM image of gold particles on polystyrene latex.

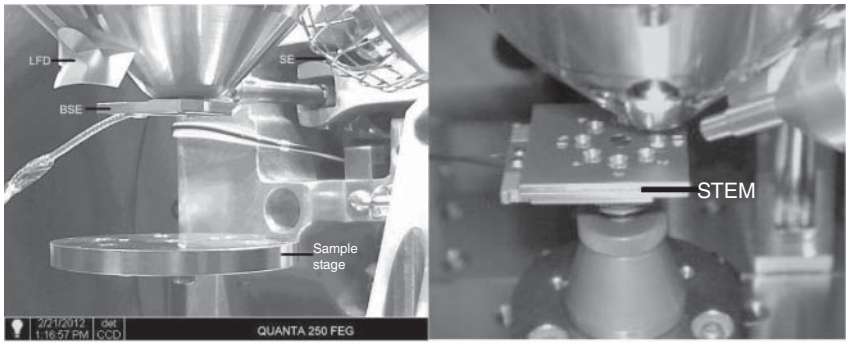

Figure 3.20 Detectors inside a SEM.

as an inert gas. Ar is ionized at high voltages. Positive Ar ions are attracted by the target and bombards it. The target is usually made of Au or Au/Pd. Target atoms are sputtered onto the sample making its surface conductive. The schematic of sputtering procedure is seen in Figure 3.21.

3.2.4.2 Environmental Scanning Electron Microscopy (ESEM)

The environmental scanning electron microscopy (ESEM) was developed in the mid-1980s, and differs from conventional SEM by changing the sample environment through a range of pressures, temperatures, and gas compositions [52]. Moist, wet, hot, dirty, oily, nonconductive samples can be examined in their natural state without modification or preparation. This technology allows imaging of samples and adds variables such as hydration, dehydration, sublimation, thermal cycling, and introduction of gas to characterize *in situ* dynamic changes such as tension, compression, deformation, crack propagation, and adhesion. Naturally hydrated samples, whose properties will change with drying, are easily character-

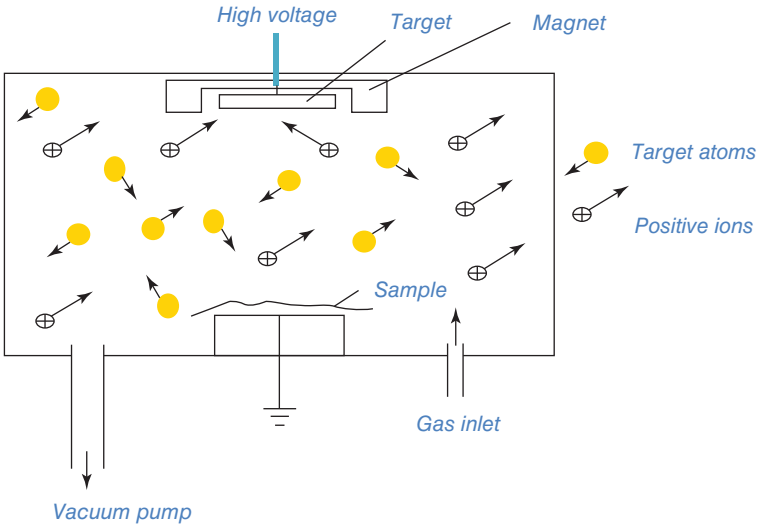

Figure 3.21 Sputter coating procedure for SEM sample preparation.

Table 3.1 The vacuum types of SEM for examined various sample type.

Vacuum types	Chamber pressure	Sample types
High vacuum	$<1.3 \times 10^{-2}$ Pa	Dry and oil free samples
Low vacuum	10–130 Pa (0.1–1 Torr)	Uncoated and nonconductive samples
ESEM vacuum	130–2600 Pa (1–20 Torr)	Moist, wet, hot, oily, and dirty samples (control humidity and temperature)

ized using water vapor and a temperature control stage. The temperature can be controlled between −25 and 1500 °C with special devices and heating, cooling, freezing, melting information of the samples can be obtained [51].

Many kinds of samples have been investigated by the electron microscopy technology using different vacuum system as shown in Table 3.1.

In conventional SEM, a single pressure limiting aperture (PLA) is used. However, multiple PLAs are used to separate the sample chamber from the column in the ESEM. In spite of the column is still high vacuum, the chamber pressures variable. By using this technique, the column and image quality do not damage the contaminants that come from the samples. At the ESEM mode, special devices such as environmental secondary electron detector (ESED) or gaseous secondary electron detector (GSED) are used for the same purpose [53].

When the electron beam goes to the nonconductive samples, positive ions are fastened on the sample surface as the charge accumulates. The gas ionization is used to amplify the SE signal. Thus, they effectively allay charging artifacts and, in this way, the specimens do not require to be coated with a conductive film. Therefore, using high accelerating voltage ESEM can acquire X-ray data from nonconductive samples [52] (Figure 3.22).

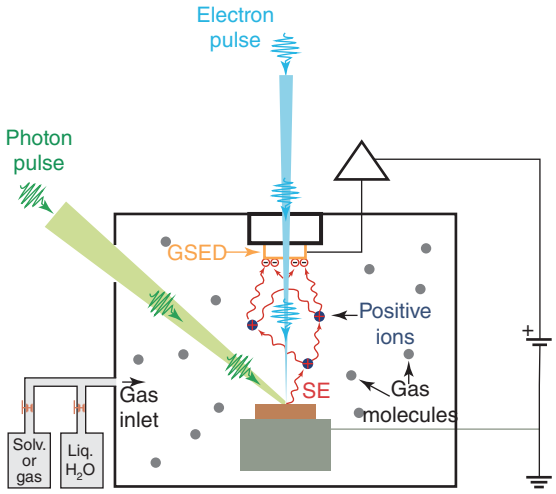

Figure 3.22 Environmental scanning electron microscope chamber with GSED detector. (Yang 2013 [53]. Reproduced with permission of Wiley.)

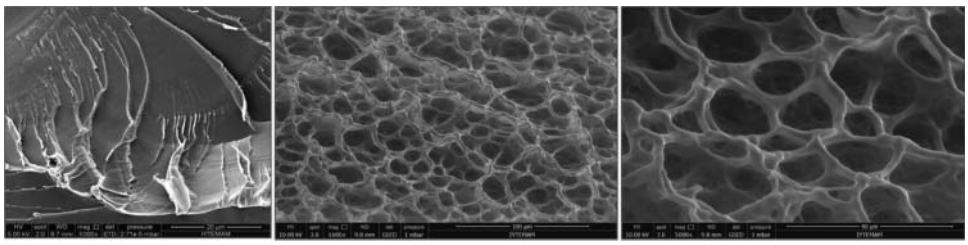

(a) (b) (c)

Figure 3.23 (a) SEM images of dried hydrogel sample with high vacuum Everhart–Thornley detector (ETD) detector. (b) SEM images of wet hydrogel sample with ESEM GSED detector. (Magnification: 1000×). (c) SEM images of wet hydrogel sample with ESEM GSED detector. (Magnification: 5000×).

At the Izmir Institute of Technology Center for Materials Research, some materials were studied by ESEM and differences between high vacuum and ESEM were showed. Hydrogels possess a highly porous structure in their wet, hydrolyzed state. Studying the pore structures of hydrogels using SEM poses challenges as the normal technique would require the use of dried samples; the material loses its pore structure when dried. Below are images comparing dry and wet samples, the latter generated with ESEM using GSED detectors (Figure 3.23).

In addition, chitosan nanoparticles have spherical shapes in wet conditions but lose this property when dried. Images from samples of dried (scanning electron microscope Everhart—Thornley detector, SEM-ETD) and wet particles are shown below. Wet samples were generated with ESEM using cooling stage and GSED detector (Figure 3.24).

3.2.4.3 Transmission Electron Microscope

Techniques using electron microscopes are very powerful because they produce high-resolution images, allowing for a wide range of applications in the fields of

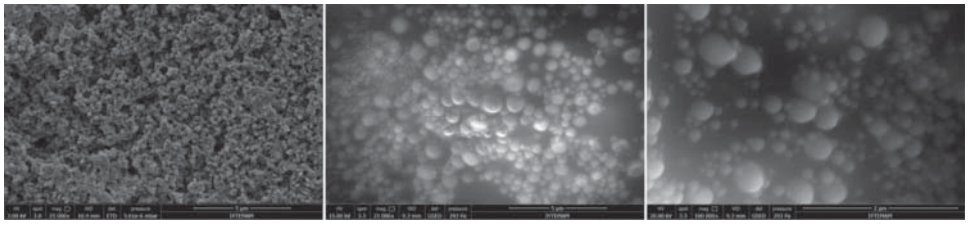

(a) (b) (c)

Figure 3.24 (a) SEM images of dried chitosan nanoparticles with high vacuum ETD detector. (b) SEM images of wet chitosan nanoparticles with ESEM GSED detector. (c) SEM images of wet chitosan nanoparticles with ESEM GSED detector with cooling stage.

education, science, and industry. With TEM, a high energy beam of electrons are used to provide morphologic, compositional, and crystallographic information on samples [54]. It is also used to collect information on characteristics such as the material's size, shape, crystallinity, composition, and elemental mapping during the interaction of the electron beam with the specimen [55].

TEM provides information to researchers on the sample at a molecular level, and is used in different fields such as nanotechnology, life sciences, medical, biological and material research, forensic analysis, gemology, and metallurgy as well as in industry and education.

The first electron microscope was developed by Knoll and Ruska at 1932. This invention earned the Nobel Prize in 1986. The first commercial TEM called The Metropolitan Vickers EM1 was built in 1936 [56].

The TEM and the light microscope operate on the same basic principles. TEM uses electrons instead of light. The wavelength of electrons is much smaller than that of light. Because of this the optimal resolution of TEM images is better than that from a light microscope. Thus, the details of the internal structure of a sample, insomuch that as small as individual atoms, can be examined. The glass lenses used in light microscopes are replaced by magnetic lenses and the projection screen is replaced by a fluorescent screen [57].

In TEM technology, a beam of high-energy electrons passes through a specimen of nanometer thickness [55]. A magnified image is obtained from the interactions of the electrons and the specimen onto the imaging device such as a fluorescent screen or a charge-coupled device (CCD) camera. The resolution of the microscope changes with different functions of the instrument such as electron source, electromagnetic lenses in the microscope column, and so on.

The comparison between light microscope, SEM, and TEM are shown in Figure 3.25 and Table 3.2.

Imaging Modes of TEM

Bright-field TEM: Images are generated by transmitted electrons. Information on the size, shape, uniformity, and dispersity of nanomaterials can be obtained.

Dark-field TEM: Diffracted electrons from crystal planes are used to image and locate defects in crystals.

H. F. Yin *et al*. showed Au-Fe_3O_4 nanoparticles from their studies with bright-field and dark-field TEM images (Figure 3.26).

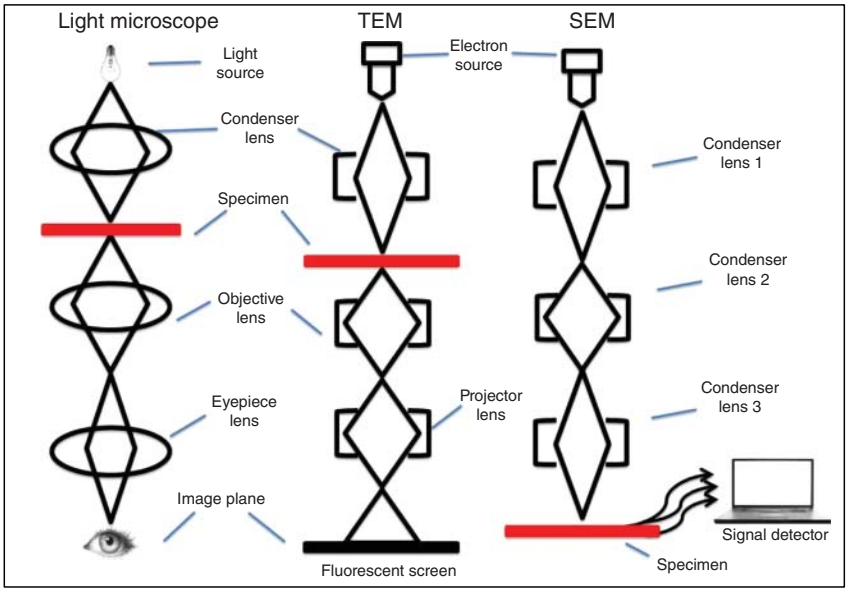

Figure 3.25 The schematic comparison between light microscope, SEM, and TEM [58].

High-resolution transmission electron microscope (HRTEM): This technique is used to study the lattice structure of crystals. When the kinetic processes of the nanomaterials are studied, the crystallinity and crystal defects can be investigated at the atomic level when changes usually begin.

Electron diffraction (ED): The symmetry and spacing of diffraction patterns can be shown by the crystal structure and phase of the sample.

In the study by X. J. Li *et al*., the microstructure of B doped diamond-like carbon (B-DLC) film is investigated mainly by HRTEM. By the preparation of proper cross-sectional specimens, HRTEM can provide more precise analysis of the structure and give direct microstructural information of the doped element in the film (Figure 3.27).

Scanning transmission electron microscope (STEM): The image is generated by raster scanning of an electron beam over the sample.

High-angle annular dark-field scanning transmission electron microscope (HAADF-STEM): It is known as *Z-contrast imaging*. STEM coupled with HAADF detector can image by the atomic number of the elements in the sample.

The study by H. Akamine *et al*. shows that the anti-phase boundaries (APBs) in the stable CoPt alloy are characterized by two atomic planes using *HAADF-STEM*. Even in TEM images, it is not possible to see something about *Z*-contrast. However, the *Z*-contrast of HAADF-STEM is highly dependent on the number and types of atoms in each atomic column (Figure 3.28).

Energy-dispersive X-ray spectroscopy (EDX or EDS): This technique is used for qualitative and quantitative elemental analysis.

Table 3.2 Comparison between light microscope–SEM–TEM.

	Light microscope	SEM	TEM
Operating environment	Air	Vacuum	Vacuum
Resolution	0.2 µm	3 nm	0.2 nm
Magnification	≤1000×	≤1.000.000×	≥1.000.000×
Source	Light	Electron gun	Electron gun
Lens type	Glass lenses	Electromagnetic lenses	Electromagnetic lenses
Viewing the sample	Eyepiece (ocular)	Digital or CCD camera	Fluorescent screen, digital or CCD camera
Usage	Simple to use	Users require technical skills	Users require technical skills and need theoretical knowledge
Electron beam		Beam focused to fine point; sample is scanned line by line	Broad, static beams
Voltages needed		Accelerating voltage much lower; not necessary to penetrate the sample (0.2–30 kV)	Need high voltage for transmission of the sample (20–1000 kV)
Specimen type	Can view both live and dead samples	Wide range of samples allowed but can view only dead samples	Sample must be very thin, can view only dead specimens
Sample preparation	Easy	Simplifies	Complicated and time consuming
Create image	An image of the sample magnified by the ocular	Beam is scanned along the surface of the sample and build up the image	Transmitted electrons are jointly focused by the objective lens and magnified to create a real image
Cost	Cheap	Expensive	Extremely expensive

Electron energy loss spectroscopy (EELS): It is more powerful than EDX. Composition of the materials and map data showing the actual element distribution in a nanostructure can be generated.

Cryo-TEM: The biological samples be imaged under cryogenic temperature. The technique allows analysing the samples at their native hydrated state of the samples at high resolution, nano to the micro-scale. For instance, Hollander and Danino used Cryo-TEM to investigate the structures of the cochleates made of dioleoylphosphatidylserine (DOPS) that are negatively charged lipid microstructures and calcium, which induce the binding of lipid layers as well as complex formation [62] (Figure 3.29).

Three-dimensional transmission electron microscope (3D-TEM): 3D images can be obtained with proper detectors and software [55].

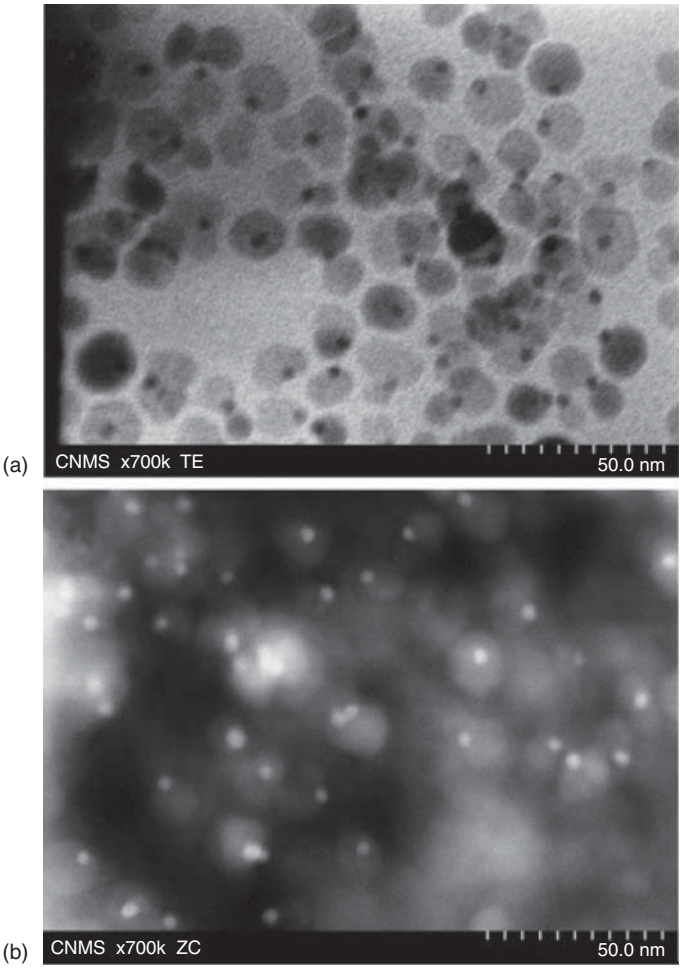

Figure 3.26 (a) Bright-field TEM image of Au-Fe_3O_4 dispersed in hexane. (b) Dark-field TEM image of Au-Fe_3O_4 dumbbells supported on SiO_2. (Yin 2008 [59]. Reproduced with permission of Royal Society of Chemistry.)

Sample Preparation of TEM The samples must be very thin (40 – 150 nm) for transmitted electrons. Some techniques of sample preparation before analyzing the specimens are given below. After these stages, the specimen places the TEM grids, support films, and SiN membranes (Figure 3.30).

- *Ultramicrotome*: To cut materials into extremely thin sections
- *Chemical and Cryo fixation* : To stabilize the materials
- *Dehydration*: To remove free water in the specimen by using organic solvent (alcohol or ethanol)
- *Embedding*: To immobilize the specimen in a hard resin-based matrix
- *Sectioning*: To obtain by slicing

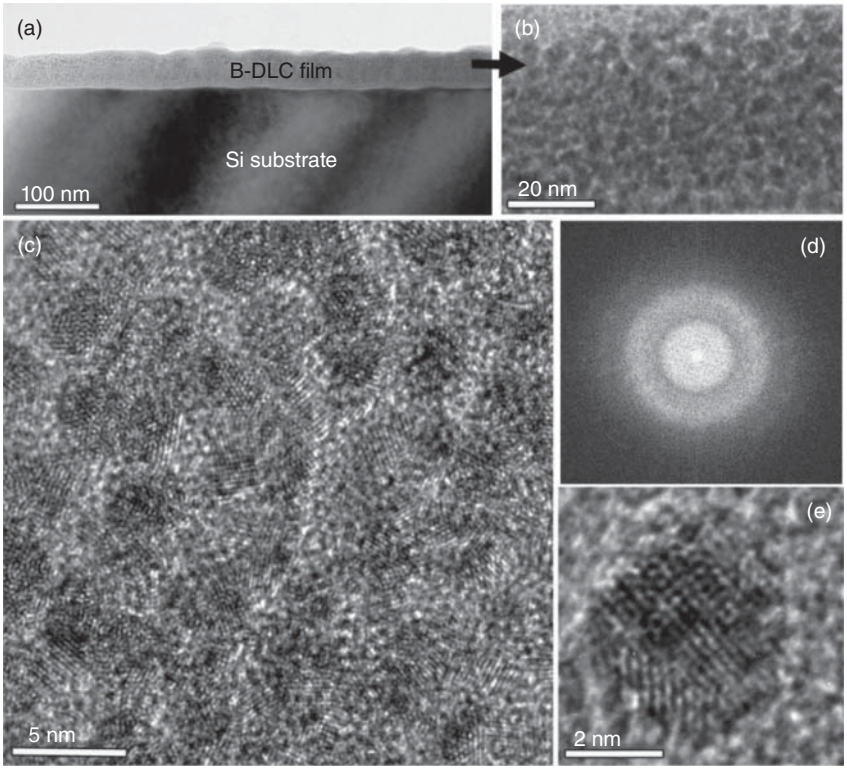

Figure 3.27 (a) Cross-sectional bright-field (BF) image of the B-DLC film; (b) the enlarged BF image of the film in (a); (c,d) HRTEM image of the film and its corresponding fast Fourier transform (FFT), showing many crystalline nanoparticles uniformly dispersed and embedded in the amorphous matrix film; and (e) HRTEM image of one of the nanoparticles in the film. (Li 2015 [60]. Reproduced with permission of American Chemical Society.)

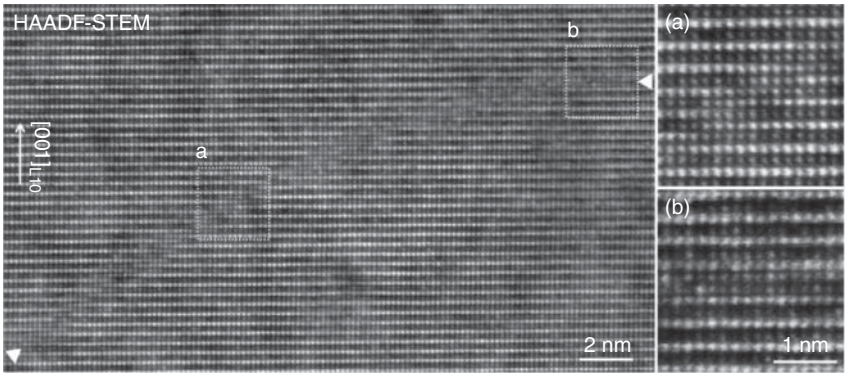

Figure 3.28 [100]L10 HAADF-STEM image of single-variant of CoPt including a single APB. Dark and bright columns correspond to Co and Pt columns, respectively. The APB starts from the lower-left corner (at white arrowhead) and curves toward the top-right corner where it follows the horizontal cubic plane. Panels (a) and (b) are enlargements of the corresponding dotted rectangles. (Akamine 2015 [61]. Reproduced with permission of Elsevier.)

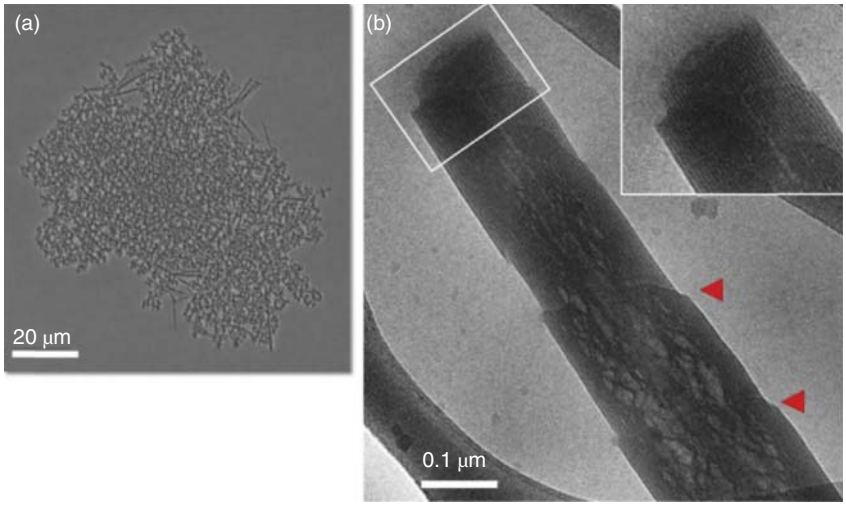

Figure 3.29 (a) Needle-like structures formed by DOPS with $CaCl_2$ detected by light microscopy. (b) Cryo-TEM image of the complex, unraveling the multilamellar structure (see also insert) and several wrapping folded layers (red arrowheads) (For interpretation of the references to color in this figure legend, the reader is referred to the web version of this article.). (Hollander 2015 [62]. Reproduced with permission of Elsevier.)

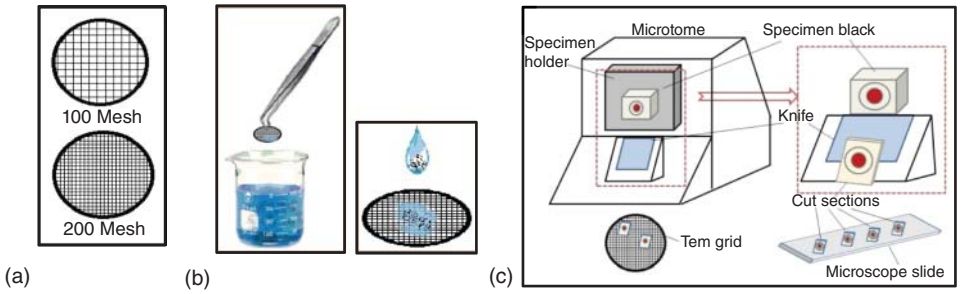

Figure 3.30 (a) Some TEM grids, (b) samples in the solution can drop directly on to the TEM grid or the TEM grid can dip into the solution, and (c) simple presentation of sample preparation with ultramicrotome [63].

- *Staining*: To enter preferentially high atomic weight metal ions into or arround the specimen that is composed of low atomic weight elements (especially biological samples)
- *Grinding and polishing*: To flatten the sample surface to be removed any damage during sectioning
- *Etching*: To generate contrast between the microstructural features of the sample surface [55, 64].

3.2.5 Scanning Probe Microscopy

Scanning probe microscope (SPM) belongs to a category of microscopes that have the ability to get atomic scale resolution images by scanning flat surfaces.

The first member of the SPM family, scanning tunneling microscope (STM) was invented by Gerd Binnig and Heinrich Rohrer at the IBM Zurich Research Laboratories in 1981 [65]. Binnig and Rohrer received the Nobel Prize in Physics in 1986 [66] for designing the STM. After the invention of atomic force microscopy (AFM) by Binnig, Quate, and Gerber in 1986 [67], SPM became one of the fundamental techniques for the surface characterization of soft materials (polymers, biological samples, etc.) and hard materials (metals, thin films, etc.)

3.2.5.1 Working Principle

Unlike optical microscopes that use light waves and electron microscopes that use electrons for imaging, SPM measures attractive or repulsive atomic forces between a sharp needle and sample surface using a spring. The spring is a microfabricated cantilever that is usually made of silicon or silicon nitride with an integrated tip. A laser beam is used to measure the deflection of the cantilever due to lowered and raised features on the sample; as the tip scans the surface in x- and y-directions over a region of interest, the focused laser beam on the cantilever is reflected due to the deflection of the cantilever and hits a position sensitive quadrant photo diode. The deflection causes slight position changes, and hence, light intensity changes on the photo diode. The difference in light intensities on the photodiode is sent to the computer control feedback loop. The feedback loop keeps the cantilever deflection constant by maintaining a constant distance between the cantilever and the sample by adjusting the voltage that is applied to the piezo scanner. The applied voltage, is then converted to a cantilever deflection in the Z-direction. Finally an accurate topographic map of the surface features is acquired. In Figure 3.31 SPM parts are seen.

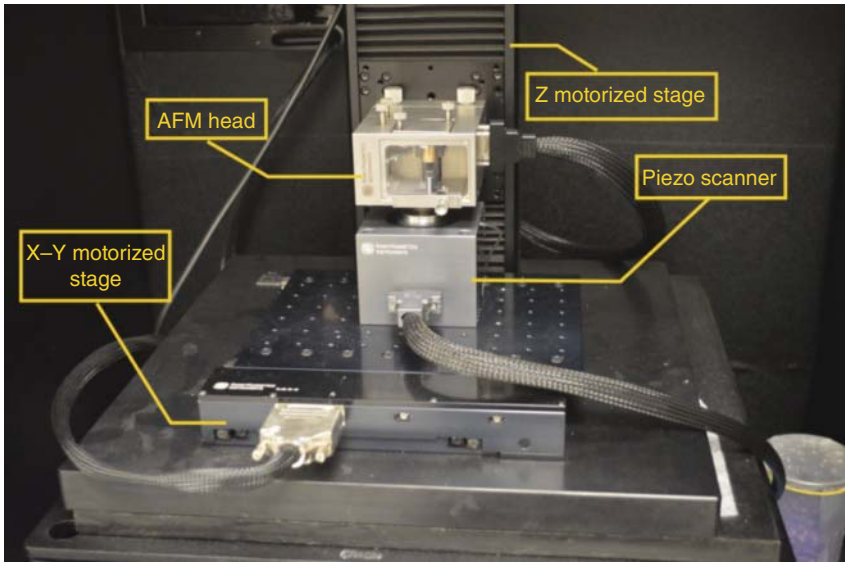

Figure 3.31 SPM scanner and stages.

3.2.5.2 Operating Modes of SPM

An SPM can be operated in the following modes:

AFM

- Contact mode AFM
- Non-contact mode AFM
- Intermittent contact mode AFM
- Closed cell liquid AFM.

STM

- Magnetic force microscope (MFM)
- Electrostatic force microscope (EFM)
- Lateral force microscope (LFM)
- Nanoindentation.

These modes of operation are being applied to a wide variety of application areas, from semiconductors to biology, from polymers to measurement of forces between particles and surfaces.

3.2.5.3 Contact Mode AFM

In the contact mode AFM, the cantilever is in physical contact with the surface. A soft cantilever with a low spring constant is used for sensitivity and low damage to the sample. Strong repulsive forces cause the cantilever to deflect while it passes over lowered and raised features. In Figure 3.32, an image acquired by contact mode AFM is seen. In contact mode AFM, hard samples and soft samples can be studied. Roy and Desai [68] determined the mechanical properties of spatially heterogeneous breast tissue specimens using contact mode AFM.

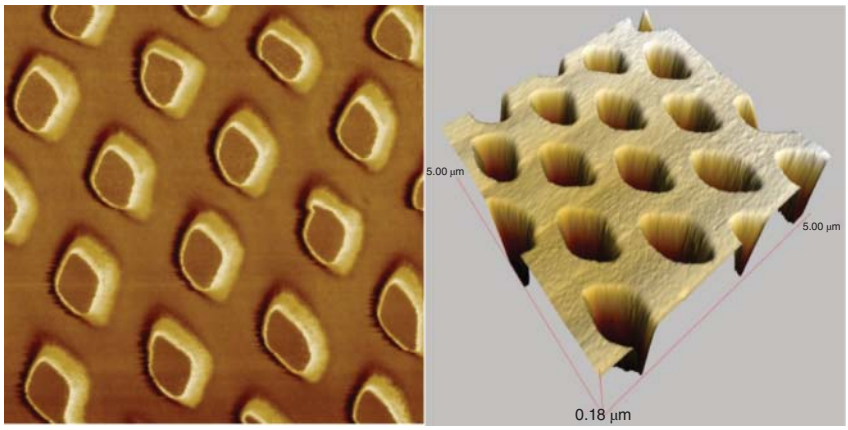

Figure 3.32 2D and 3D contact mode AFM image of platinum coated array. (Image Courtesy of Gökhan Erdoğan.)

3.2.5.4 Noncontact Mode AFM

In the noncontact mode AFM, the cantilever is not in physical contact with the surface. For sensitivity and low damage to the sample, stiff cantilevers with a high spring constant are used. Cantilever oscillates at its resonance frequency using a feedback loop. The feedback loop prevents the cantilever from crashing into the surface. The oscillation amplitude of the cantilever decreases when the tip approaches the sample surface. The feedback loop corrects these amplitude deviations in order to retrieve topographical information from the sample surface. Guillermet *et al*. [69] imaged single decastarphene molecules, adsorbed on Cu(1 1 1) and on a bilayer of NaCl/Cu(1 1 1) by using noncontact mode AFM.

3.2.5.5 Intermittent Contact Mode AFM

In the intermittent contact mode AFM, the cantilever is occasionally in physical contact with the surface. For sensitivity and low damage to the sample, stiff cantilevers with a high spring constant is used. The cantilever oscillates at its natural resonance frequency using a fixed frequency signal source. The oscillation amplitude is higher than that of a noncontact mode. The forces between the sample and the surface change the oscillation amplitude and the relative phase of the resultant oscillations. The bigger oscillations make the deflection signal large enough for the feedback circuit, which keeps the root mean square (RMS) amplitude constant by measuring the phase shifts and RMS amplitude of the vibrations. In Figure 3.33, intermittent contact mode AFM image of a CCD camera sensor is seen. Turkan and Guden [70] investigated the effects of alkali and nitric acid surface treatment and acid etching on the CaP deposition used for biomedical applications. They measured and compared the surface roughness of the samples using intermittent contact mode AFM. 2D and 3D AFM images of surface-treated samples are seen in Figure 3.34.

3.2.5.6 Closed Cell Liquid AFM

Apart from other modes of operation, closed cell liquid AFM is the most important mode due to its ability to operate under aqueous solutions. Attractive forces are eliminated due to surface tension, which enables the sample surface to be examined with a minimum cantilever tip force. It is an ideal case for imaging biological specimens and soft materials. There are some difficulties in this method such as performing good sealing, avoiding air bubbles that cause trouble in focusing the laser beam properly, maintaining the immobility of the sample, and minimizing laser refractions while passing through air-liquid interfaces. The procedures for imaging samples under liquid are the same as that for Contact Mode AFM and Intermittent Contact Mode AFM. Campen *et al*. [71] studied the *in situ* formation and properties of self-assembled films formed on mica surfaces by octadecylamine from alkane solution using liquid cell AFM.

3.2.5.7 STM

STM is based on electron tunneling that is a quantum mechanical phenomenon. In this method the sample must be conductive because a bias voltage is applied between the tip and the sample surface. The biased tip scans the surface while the tunnel current is present. There are two modes in this operation. The first one is

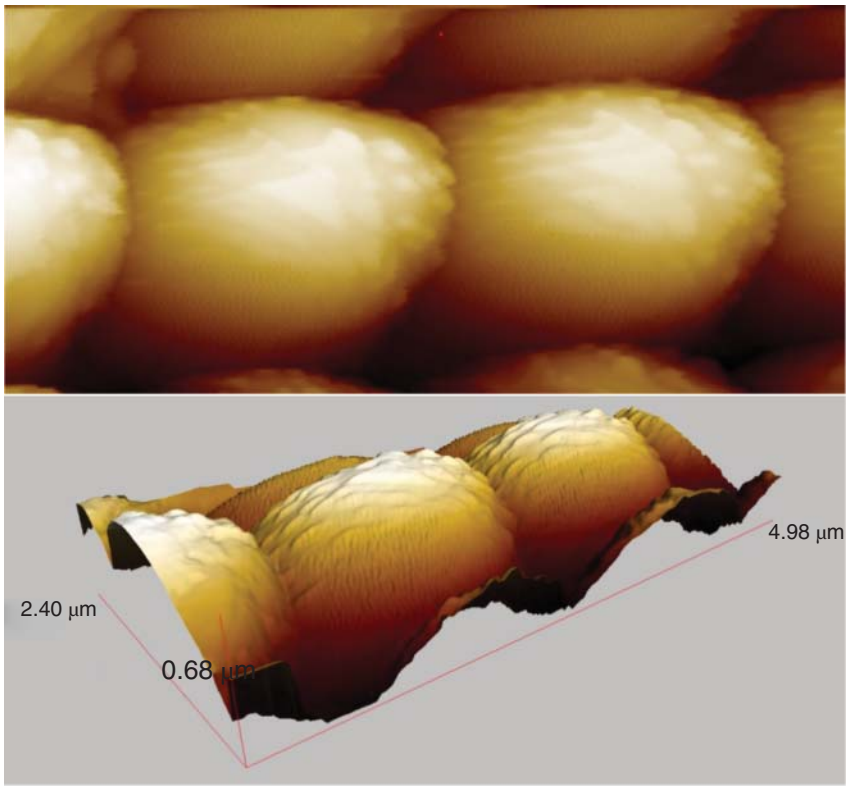

Figure 3.33 2D and 3D intermittent contact mode AFM image of a CCD camera sensor. (Image Courtesy of Gökhan Erdoğan.)

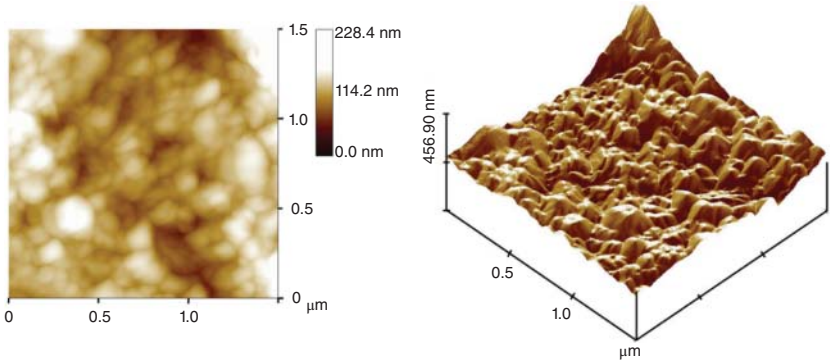

Figure 3.34 2D and 3D intermittent mode AFM images of surface topologies of foam specimen. (Image Courtesy of Uğur Türkan.)

the constant height mode in which the distance between the tip and the surface is kept constant using a feedback circuit. The second one is the constant current mode in which the tunneling current is kept constant using a feedback circuit. The feedback circuit supplies appropriate voltage to the scanner piezo, which moves the tip with picometer resolution up and down to keep the tunneling current constant. Shin *et al*. [72] studied the geometric and electronic structures of Fe islands on MgO film layers with STM.

3.2.5.8 MFM

MFM is a mode that maps the magnetic force gradient above the sample surface. In this mode, the cantilever must be coated with a thin magnetic film and the sample must have magnetic properties. There are two scans in this mode. The first scan is used to determine the topography while the second one is used to determine the magnetic force gradient. Varghese *et al*. [73] reported a new methodology to obtain reliable correlation between magnetic cluster details by using MFM.

3.2.5.9 EFM

EFM is a mode that maps conductive and nonconductive gradient above the sample surface. The cantilever must be coated with a conductive film. A voltage is applied between the sample and the tip in order to adjust the strength of the electric interaction between the tip and the sample. The first scan is used to determine the topography while the second one is used to determine the electrostatic state of the sample surface. Kazakova *et al*. [74] presented local electrical characterization of epitaxial graphene grown on both Si- and C-faces of 4H-SiC using electrostatic force microscopy. In another study, Pruneanu *et al*. [75] organized metallic nanoparticles into one-dimensional assemblies by using DNA as a "template" and allowing the preparation of various silver nanostructures. They demonstrated this study by employing EFM.

3.2.5.10 LFM

LFM measures frictional forces between the tip and the sample surface by measuring the tip deflection in lateral direction and, therefore, it can give information about the areas with varied friction. Taran *et al*. [76] used LFM techniques to determine the molecular-scale characteristics of friction forces between silica particles and silica wafers in aqueous solutions.

3.2.5.11 Nanoindentation

Nanoindentation measures the mechanical properties and wear characteristics of soft and hard materials such as thin films and polymers. It measures these properties by indenting the tip into the sample and measuring the force and distance curves. Enax *et al*. [77] characterized the mechanical properties such as stiffness and hardness of shortfin mako shark teeth using nanoindentation. Tekaya *et al*. [78] used nanoindentation and nanoscratch tests to characterize the mechanical and tribological properties of Ti/TiN multilayer and monolithic TiN nanocoatings.

3.2.6 Contact Angle

Wetting is an important parameter for a wide range of industrial and daily applications including self-cleaning, anti-icing, anti-wetting, and more. Contact angle measurement is used to determine surface wettability and the contact angle represents the value of wettability. Theoretically, the contact angle values must be between 0° and 180°. If the contact angle is less than 90°, these surfaces are called *hydrophilic*. If the wetting angle is higher than 90°, these kind of surfaces can be classified as water hydrophobic. When the contact angle approaches to 180°, the surface is considered superhydrophobic.

It is well known that the contact angle depends on surface chemistry (Cassie model [79]) and surface topography (Wenzel model [80, 81]). Therefore, apart from wetting properties of the surface, some other chemical, physicochemical, and morphological properties can be learned/perceived from the contact angle measurement. For instance, the surface free energy of solids can be calculated using contact angle measurements [82–84].

There are several ways to measure the contact angle. Among them, the contact angle goniometer is the most common technique (Figure 3.35). In this method, a drop is placed on the solid surface by a syringe that can be operated manually or automatically. Then, the image of the drop on the surface is magnified and captured by the camera. Finally, the angle of incidence between the liquid–surface interface and the liquid–vapor interface, namely, the contact angle, is measured by means of software. A contact angle goniometer device enables a direct, easy, and efficient contact angle measurement. However, if the sample surface area is smaller than that of the water drop or if the substrate has a porous structure, this method cannot be used. In such cases, other measurement methods such as Washburn's equation capillary rise and thin-layer wicking methods can be used in order to overcome these handicaps [85, 86]. Therefore, depending on the physical properties of the sample, the most suitable contact angle measurement technique should be chosen.

The dynamic contact angle is another important definition, which is related to wettability. It refers to the *advancing angle* and the *receding contact angle* (Figure 3.36). As liquid is added to the drop on the surface, the contact angle approaches a maximum value. This maximum angle is called *advancing contact angle*. When liquid is withdrawn from the drop, the contact angle decreases to a minimum value. This minimum contact angle is called *receding contact*

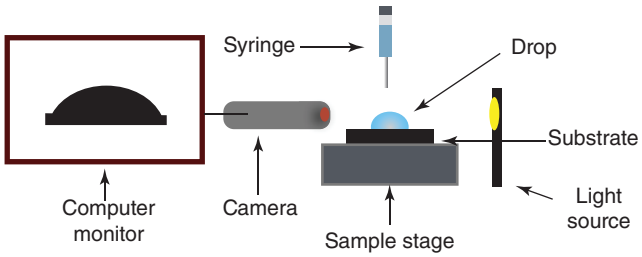

Figure 3.35 Schematic diagram of contact angle goniometer device.

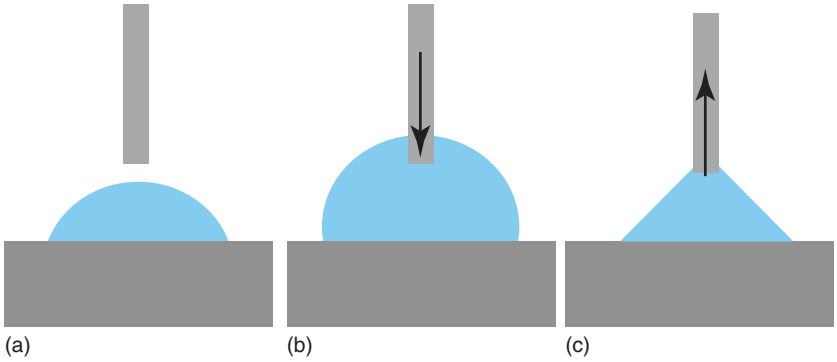

Figure 3.36 (a) Static contact angle, (b) advancing contact angle, and (c) receding contact angle.

angle. Contact angle hysteresis is the difference between the advancing contact angle and receding contact angle. Contact angle hysteresis gives a rich source of surface properties such as surface chemistry, morphology, contamination, adhesive properties, and so on.

3.2.7 BET (Brunauer–Emmett–Teller) Analysis

The Brunauer, Emmett, and Teller (BET) analysis, which is the most common method for measuring the specific surface area of a material, involves calculating the amount of adsorbate gas against the relative vapor pressure of inert gases at a variety of conditions. Nitrogen gas is generally used as the gas adsorptive molecule because of its inert nature property. In the analysis, nitrogen gas is exposed to solid materials under investigation at liquid nitrogen conditions (i.e., 77 K).

In the BET analysis, a sample is degassed prior to the surface analysis to help remove water and possible absorbed molecules. The degassed sample is weighed and then employed for analysis in an analysis compartment. Nitrogen gas is used for the analysis because of its inert nature property. The entire sample tube is immersed in a coolant bath of liquid nitrogen exposing it to lower temperature. A purge nitrogen gas is slowly adsorbed on the solid material and the relative vapor pressure of nitrogen is recorded against the volume of adsorbate by using the computer program of the BET analyzer. The connection between the relative vapor pressure and the amount of adsorbed at constant temperature is called *adsorption isotherm*. In BET analysis, the interpretation of adsorption isotherm is useful for the calculating the surface area of the material and understanding the pore structure of the material. The types of isotherm, which have been classified by UIPAC in 1985, are presented in Figure 3.37 [87]. Type I is characterized by a microporous solid (pore widths below 2 nm). Type II isotherm, which represents unrestricted monolayer–multilayer adsorption, is an indicative of nonporous or macroporous materials. Type III and V isotherms result from weak interactions between solid and gas molecules. Type IV isotherms occur on materials that possesses mesopore structure (pore widths from 2 to 50 nm). The most characteristic

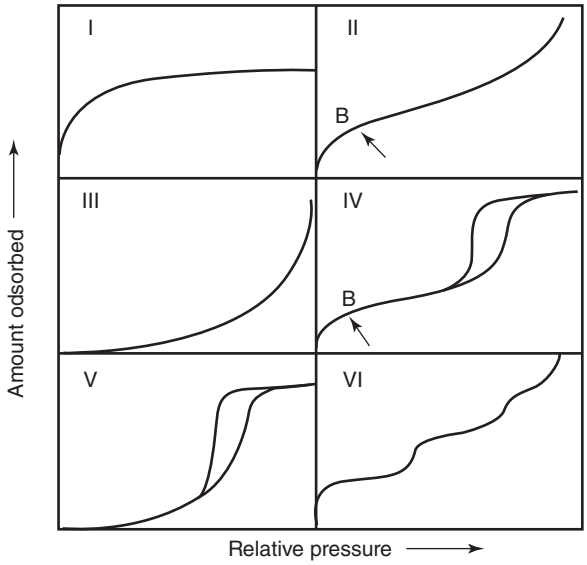

Figure 3.37 The six types of adsorption isotherm according to the 1985 IUPAC classification [87].

features of the Type IV and V isotherms are the hysteresis loops which result from the capillary condensation effect [88]. Type VI exhibits a stepwise multilayer adsorption on a nonporous surface [89].

The surface area of the material is determined from the evaluation of the adsorption isotherm data that is obtained from the BET analysis. Langmuir and BET model equations are applied to the isotherm data for this purpose.

The Langmuir model equation describes microporous material exhibiting Type I isotherms [90]. This model assumes that:

- Monolayer adsorption
- Energetically uniform surface
- No interactions between adsorbed species.

The form of the Langmuir equation is:

$$P/P_0V = 1/bV_m + P/P_0V_m \tag{3.11}$$

where V is the volume of adsorbed vapor, V_m is the volume of monolayer, P is the partial pressure of the adsorbate, P_0 is the saturation vapor pressure of the adsorbate, and b is the constant.

A plot of P/P_0V versus P/P_0 gives slope $= 1/V_m$ and intercept $= 1/bV_m$. The values of V_m and Langmuir constant b are determined from the slope of intercept of the Langmuir equation plot.

The surface area of the material is determined from

$$S = V_m \times N \times A_x/M \tag{3.12}$$

where A_x is the cross sectional adsorbate area, N is the Avagadro number, V_m is the volume of monolayer, and M is the molar volume of gas.

BET equation model, which is the extension of the Langmuir theory, is applicable to Type II and IV isotherms [91]. Type II isotherm describes unrestricted

multilayer formation whereas Type IV isotherm is indicative of restricted multilayer formation. BET equation model assumes the following [91]:

1) Gas molecules physically adsorb on a solid in layers infinitely
2) There is no interaction between each adsorption layer
3) The Langmuir theory can be applied to each layer.

The form of the BET model equation is:

$$\frac{P}{V[P_0 - P]} = \frac{1}{V_m C} + \frac{C-1}{V_m C}\frac{P}{P_0} \tag{3.13}$$

where V is the volume of adsorbed vapor, V_m is the volume of monolayer, P is the partial pressure of the adsorbate, P_0 is the saturation vapor pressure of the adsorbate, and C is the constant.

A plot of $P/(P_0 - P)V$ versus P/P_0 gives slope $= C - 1/V_m C$ and intercept $= 1/CV_m$. The values of V_m and BET constant C are determined from the slope of intercept of the BET equation plot. For BET surface area measurements, relative pressures are in the range of $0.05 \leq P/P_0 \leq 0.30$. At higher relative pressures BET equation is invalid for occurrence of the capillary condensation effect. At lower relative pressure values ($P/P_0 < 0.05$), the amount of adsorbed gas is too small to be measured. The surface area of the material is determined from the Eq. (3.5).

In the literature, BET analysis was performed to measure the surface area of different materials, which is important information for industrial applications such as catalyst, adsorbent, ion exchanger, heat insulator, and so on. Sand, clay, organo-clays, and cotton fibers that were used in the clean-up operation of oil/fuel spills were characterized by N_2 adsorption–desorption and their isotherms are given in Figure 3.38 [92]. The adsorption isotherm of the materials exhibited a Type II and IV isotherm, which described unrestricted and restricted multilayer formation, respectively. The BET surface areas of the materials calculated from BET model equation and their values varied from 1.2 to 27.1 $m^2 g^{-1}$.

3.2.8 Terahertz Time Domain Spectroscopy

Terahertz time domain spectroscopy (THz-TDS) is a very promising method for a wide range of applications. This spectroscopic technique uses THz waves generated and detected by far IR pulses. The electromagnetic waves have the frequencies 0.1–10 THz known as *THz waves* or *T-rays*. This regime falls between the IR and microwave regions of the electromagnetic spectrum (Figure 3.39). THz beams can be manipulated by optical components such as mirror and lens and the phase of the electric field can be measured; therefore, THz region combines electronic and optic spectrum.

Terahertz radiation is nonionizing and can pass through plastic, paper, wood, and ceramics. But it cannot penetrate metal or liquid water. There are two common methods used in the generation of pulsed THz beams. They are photoconductivity (PC) and optical rectification (OR) methods. In the photoconductivity method, THz pulses are generated by illuminating the semiconductor material

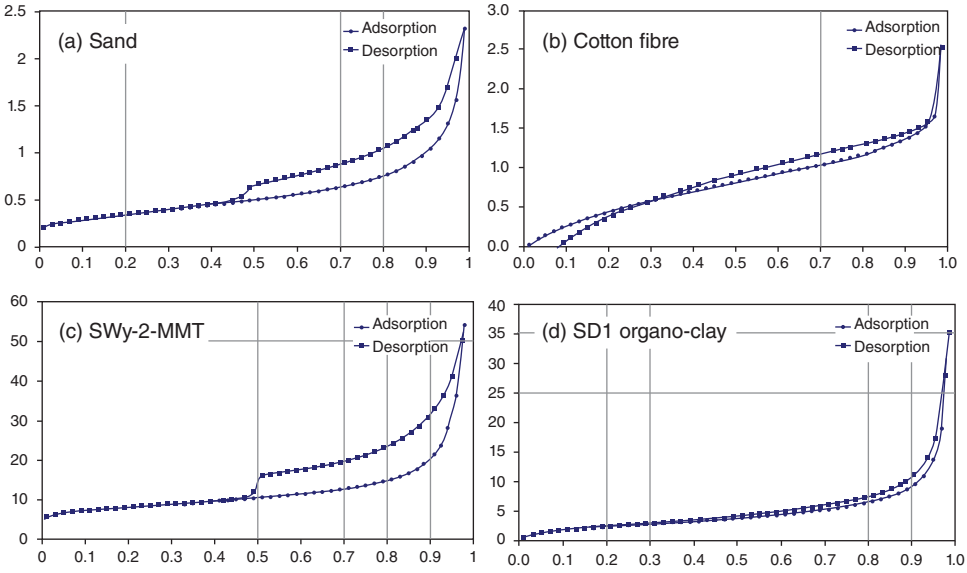

Figure 3.38 N_2 adsorption isotherms for (a) sand, (b) cotton fiber, (c) Swy-2-montmorillonite (MMT) (clay), and (d) SD1 organo-clay, vertical axis: volume adsorbed ($cm^3\ g^{-1}$ STP); horizontal axis (P/P_0). (Carmody 2007 [92]. Reproduced with permission of Elsevier.)

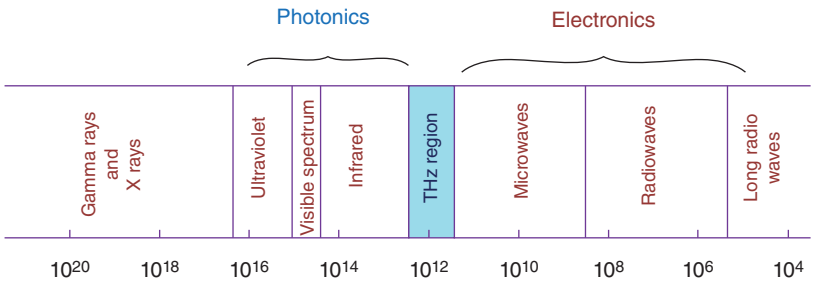

Figure 3.39 The electromagnetic spectrum. THz radiation is in the transition region between electronics and photonics.

with a femtosecond laser pulse [93]. This technique is also used in the detection of THz waves. Low-temperature grown GaAs (LT-GaAs) have short carrier life time, high mobility, and high resistivity and, therefore, are attractive for THz generation and detection [94, 95]. THz wave generation via optical reflection (OR) is method based on difference frequency mixing and materials that have large second order susceptibility $\chi^{(2)}$ is used for this method [96]. ZnTe is the most favorable electro-optic material for generation of the THz beam because of its large coherence length of 0.8 µm, which is important for the OR method [96]. But also DAST [97], GaP [98], $LiNbO_3$, ZnSe, CdS [99] are used to generate THz radiation. The peak electric field is higher in the PC method than in OR. However, terahertz beams generated by the OR technique has an extraordinary bandwidth.

The frequencies of the electromagnetic waves are too high to be measured digitally using electronic counters and there are two techniques that are frequently used to measure the wave form of terahertz pulses: the PC method [100] and electroopting sampling (EO). The PC method detects THz waves by a similar mechanism used in the generation by the PC method. EO sampling is based on the Pockells effect and was investigated by many researchers [96, 101]. A comparison of these two detection methods can be found in [102].

Pulsed terahertz waves generated and detected by these methods are used in the THz-TDS. Before the advent of THz-TDS, the most widely used method was the Fourier transform spectroscopy (FTS). FTS is only sensitive to the amplitude of the wave but THz-TDS is a phase-sensitive method and, therefore, both the amplitude and the phase of the electric field can be measured directly. The real and imaginary parts of the dielectric function can be obtained without using Kramers–Kronig relations. Another advantage of the THz-TDS technique is the high signal to noise ratio (S/N) in the range of 10 GHz to 4 THz. The field amplitude S/N is 10^4 in this range while FTS is about 300 [103]. There are two different configurations that are generally used for THz-TDS: transmission and reflection. In the case of strongly reflective and optically thick samples, reflection measurements are necessary. In terahertz time domain reflection spectroscopy [104], the complex refractive index of the material is obtained by taking the ratio of Fourier transformed electric field of the sample and the reference mirror. The surface of the mirror must be positioned at the same place as that of the sample. Any difference between the sample and reference mirror (>1 μm) results in a severe error in the phase measurement and, thereby, in the complex refractive index [105].

If the sample is optically thin and transparent or semi-transparent in the THz region, it is convenient to use terahertz time domain transmission spectroscopy [106]. In terahertz time domain transmission spectroscopy, the electric field of the THz waves is measured in the absence of the sample $E_{\mathrm{ref}}(t)$ and in the presence of the sample $E_{\mathrm{sam}}(t)$. $E_{\mathrm{ref}}(t)$ and $E_{\mathrm{sam}}(t)$ are Fourier transformed and the transmission function is calculated by taking the ratio of $\tilde{E}_{\mathrm{sam}}(\omega)$ and $\tilde{E}_{\mathrm{ref}}(\omega)$ [107].

$$\begin{aligned}\frac{\tilde{E}_{\mathrm{sam}}(\omega)}{\tilde{E}_{\mathrm{ref}}(\omega)} &= |\sqrt{T(\omega)}|\ \exp\left\{-i\left[\Delta\varphi(\omega)-\frac{\omega}{c}d\right]\right\} \\ &= \frac{4\tilde{n}(\omega)}{[\tilde{n}(\omega)+1]^2}\frac{\exp\left\{-i[\tilde{n}(\omega)-1]\frac{\omega}{c}d\right\}}{1-\frac{[\tilde{n}(\omega)-1]^2}{[\tilde{n}(\omega)+1]^2}\exp\left[-i2\tilde{n}(\omega)\frac{\omega}{c}d\right]}\end{aligned} \tag{3.14}$$

where $\tilde{n}(\omega) = n(\omega) - ik(\omega)$ is the complex refractive index of the sample, c is the speed of light, d is the thickness of the sample, $T(\omega)$ and $\Delta\varphi$ are the power transmittance and the phase shift due to the sample respectively. $n(w)$ and $k(w)$ can be determined by using experimentally obtained $\sqrt{T(\omega)}$ and $\Delta\varphi$. The complex dielectric constant $\tilde{\varepsilon}(\omega) = \varepsilon(\omega) - i\varepsilon(\omega)$ which is related to the complex refractive index by the relation $\tilde{\varepsilon} = \tilde{n}^2(\omega)$ can be calculated.

The experimental setups for terahertz time domain transmission spectroscopy is shown in Figure 3.40. In the first system (Figure 3.40a), a THz beam is generated and detected by photoconductive antenna, which consists of two metal striplines

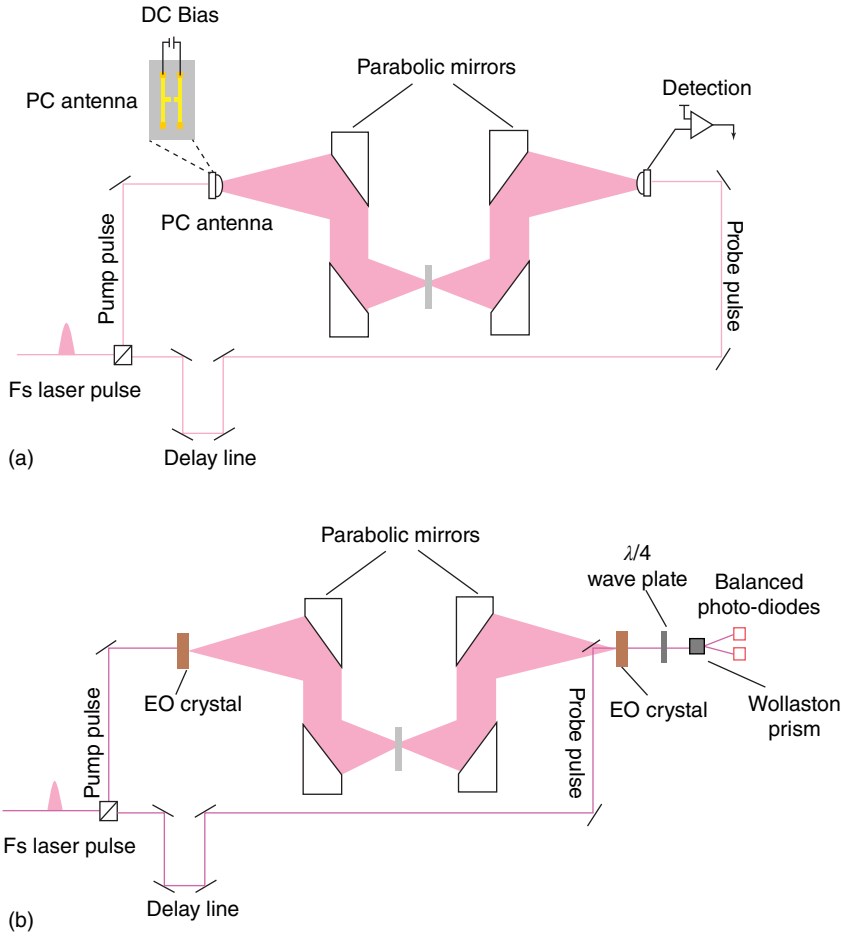

Figure 3.40 The experimental setups for terahertz time domain transmission spectroscopy. Terahertz pulses are generated and detected by (a) photoconductive antenna and (b) electro-optic material.

deposited on a semiconductor material. Laser pulse is splitted into the probe and pump pulse by the beam splitter. Pump pulse incident onto the PC antenna and generates electron-hole pairs. Acceleration of the charge carriers under the DC bias field gives rise to a transient current, and this time-dependent current radiates THz waves. The emitted radiation is focused onto the sample by parabolic mirrors. After passing through the sample, THz pulses are incident onto the second PC antenna and accelerate the photocarriers generated by the probe pulse. The transient current is proportional to the electric field of the terahertz pulse. By changing the time delay between the probe and the pump pulse THz wave form is obtained.

In the second system (Figure 3.40b) electro-optic crystals are used for generation and detection of THz beams. A femtosecond laser pulse that contains a range of frequencies interacts with the electrooptic material and THz waves are

generated by frequency beating. After passing through the sample THz waves are focused onto another electrooptic crystal with the laser pulse at the same time. The frequency of the optical pulse is higher than the THz pulse and, therefore, the electric field of the terahertz beam serves as a static field and induces a small birefringence in the crystal. Linearly polarized probe beams gain a small elliptical polarization that is proportional to the electric field of the terahertz waves. The quarter wave plate induces a phase shift and the Wollaston prism splits the probe beam into the s and p polarization components. The difference between these components is measured by a balanced photodetector. Terahertz waveform is obtained by changing the time delay between the probe and the pump pulse.

THz-TDS is a powerful technique and it is widely used in material characterization [108], biomedical research [109], imaging [110], security [111], and communication applications [112].

References

1 History http://www.history.com/this-day-in-history/german-scientist-discovers-x-rays (accessed 20 April 2016).
2 Niemantsverdriet, J.W. (2007) *Spectroscopy in Catalysis*, John Wiley & Sons, Inc..
3 Robinson, J.W. (1974) *Handbook of Spectroscopy*, CRC Press, Cleveland, OH.
4 Kelsall, R.W., Hamley, I.W., and Geoghegan, M. (eds) (2005) *Nanoscale Science and Technology*, John Wiley & Sons, Ltd., Chichester.
5 Bubert, H., Rivière, J.C., Arlinghaus, H.F., Hutter, H., Jenett, H., Bauer, P., Palmetshofer, L., Fabry, L., Pahlke, S., Quentmeier, A., and Hinrichs, K. (eds) (2002) *Surface and Thin-Film Analysis*, Wiley-VCH Verlag GmbH & Co. KGaA.
6 Tang, W.-W., Dong, F., Wong, K.-H., and Wang, Y. (2015) Preparation, characterization and in vitro release of zein–pectin capsules for target delivery. *Curr. Drug Delivery*, **12**, 397–405.
7 Gupta, A., Kaur, C.D., Saraf, S., and Saraf, S. (2016) Formulation, characterization, and evaluation of ligand-conjugated biodegradable quercetin nanoparticles for active targeting. *Artif. Cells Nanomed. Biotechnol.*, **44**, 960–970.
8 Vidigal, G.M., Groisman, M., de Sena, L.A., and de Almedia Soares, G. (2009) Surface characterization of dental implants coated with hydroxyapatite by plasma spray and biomimetic process. *Implant Dent.*, **18**, 353–361.
9 Liu, K.-Z., Shi, M.-H., and Mantsch, H.H. (2005) Molecular and chemical characterization of blood cells by infrared spectroscopy: a new optical tool in hematology. *Blood Cells Mol. Dis.*, **35**, 404–412.
10 Güler, G., Gärtner, R.M., Ziegler, C., and Mäntele, W. (2016) Lipid-protein interactions in the regulated betaine symporter BetP probed by infrared spectroscopy. *J. Biol. Chem.*, **291**, 4295–4307.
11 Movasaghi, Z., Rehman, S., and Rehman, I.U. (2008) Fourier Transform Infrared (FTIR) spectroscopy of biological tissues. *Appl. Spectrosc. Rev.*, **43**, 134–179.

12 Belfer, S., Fainchtain, R., Purinson, Y., and Kedem, O. (2000) Surface characterization by FTIR-ATR spectroscopy of polyethersulfone membranes-unmodified, modified and protein fouled. *J. Membr. Sci.*, **172**, 113–124.

13 Mäntele, W. (2012) *Biophysik*, 1st edn, Eugen Ulmer Verlag, Stuttgart.

14 Barth, A. (2007) Infrared spectroscopy of proteins. *Biochim. Biophys. Acta*, **1767**, 1073–1101.

15 Güler, G. (2013) Investigation of structural and functional properties of the betaine transporter BetP from Corynebacterium glutamicum by using infrared spectroscopy. Doctora thesis, pp. 1–165.

16 Dubal, D.P., Lee, S.H., Kim, J.G., Kim, W.B., and Lokhande, C.D. (2012) Porous polypyrrole clusters prepared by electropolymerization for a high performance supercapacitor. *J. Mater. Chem.*, **22**, 3044–3052.

17 Chung, I.-M., Park, I., Seung-Hyun, K., Thiruvengadam, M., and Rajakumar, G. (2016) Plant-mediated synthesis of silver nanoparticles: their characteristic properties and therapeutic applications. *Nanoscale Res. Lett.*, **11**, 40.

18 Gürsoy, M., Uçar, T., Tosun, Z., and Karaman, M. (2016) Initiation of 2-hydroxyethyl methacrylate polymerization by tert-butyl peroxide in a planar PECVD system. *Plasma Processes Polym.*, **13**, 438–446.

19 Ding, B., Jasensky, J., Li, Y., and Chen, Z. (2016) Engineering and characterization of peptides and proteins at surfaces and interfaces: a case study in surface-sensitive vibrational spectroscopy. *Acc. Chem. Res.* doi: 10.1021/acs.accounts.6b00091

20 Hu, Q., Suzuki, H., Gao, H., Araki, H., Yang, W., and Noda, T. (2003) High-frequency FTIR absorption of SiO2/Si nanowire. *Chem. Phys. Lett.*, **378**, 299–304.

21 Noda, T., Suzuki, H., Araki, H., Yang, W., Shi, Y., and Tosa, M. (2005) Microstructures and IR spectra of long amorphous SiO2/Si nanowires. *Appl. Surf. Sci.*, **241**, 231–235.

22 Nagai, N. and Hashimoto, H. (2001) FT-IR-ATR study of depth profile of SiO2 ultra-thin films. *Appl. Surf. Sci.*, **172**, 307–311.

23 Laroche, G., Fitremann, J., and Gherardi, N. (2013) FTIR-ATR spectroscopy in thin film studies: the importance of sampling depth and deposition substrate. *Appl. Surf. Sci.*, **273**, 632–637.

24 Gunasekaran, S., Anbalagan, G., and Pandi, S. (2006) Raman and infrared spectra of carbonates of calcite structure. *J. Raman Spectrosc.*, **37**, 892–899.

25 Boronat, A., Silvestre, S., and Castañer, L. (2013) Optical and compositional characterization of GaAs(Ti) thin films deposited by R.F. magnetron sputtering. *J. Non-Cryst. Solids*, **359**, 21–26.

26 Pusep, Y., Milekhin, A., and Poropov, A. (1993) FTIR-spectroscopy of (GaAS)n/(AlAs)m superlattice. *Superlattices Microstruct.*, **13**, 115–123.

27 Pusep, Y., Milekhin, A., and Poropov, A.I. (1994) FTIR spectroscopy of longitudinal confined phonons and plasmon-phonon vibrational modes in GaAsn/AlAsm superlattices. *Solid State Electron.*, **37**, 613–616.

28 Juang, F.-S., Su, Y.-K., Yu, H.H., and Liu, K.-J. (2003) Characterization of the InAsSb/GaSb superlattices by Fourier transform infrared spectroscopy. *Mater. Chem. Phys.*, **78**, 620–624.

29 Catauro, M., Papale, F., and Bollino, F. (2015) Characterization and biological properties of TiO2/PCL hybrid layers prepared via sol–gel dip coating for surface modification of titanium implants. *J. Non-Cryst. Solids*, **415**, 9–15.

30 Tamosaityte, S., Galli, R., Uckermann, O., Sitoci-Ficici, K.H., Later, R., Beiermeister, R., Doberenz, F., Gelinsky, M., Leipnitz, E., Schackert, G., Koch, E., Sablinskas, V., Steiner, G., and Kirsch, M. (2015) Biochemical monitoring of spinal cord injury by FT-IR spectroscopy--effects of therapeutic alginate implant in rat models. *PLoS One*, **11**(2), e0150237.

31 Malakauskaite-Petruleviciene, M., Stankeviciute, Z., Niaura, G., Garskaite, E., Beganskiene, A., and Kareiva, A. (2016) Characterization of sol-gel processing of calcium phosphate thin films on silicon substrate by FTIR spectroscopy. *Vib. Spectrosc.*, **85**, 16–21.

32 Güler, G., Džafić, E., Vorob'ev, M.M., Vogel, V., and Mäntele, W. (2011) Real time observation of proteolysis with Fourier transform infrared (FT-IR) and UV-circular dichroism spectroscopy: watching a protease eat a protei. *Spectrochim. Acta, Part A*, **79**, 104–111.

33 Güler, G., Vorob'Ev, M.M., Vogel, V., and Mäntele, W. (2016) Proteolytically-induced changes of secondary structural protein conformation of bovine serum albumin monitored by Fourier transform infrared (FT-IR) and UV-circular dichroism spectroscopy. *Spectrochim. Acta, Part A*, **161**, 8–18.

34 Fabian, H. and Mäntele, W. (2002) Infrared spectroscopy of proteins, in *Handbook of Virational Spectrosopy* (eds J.M. Chalmers and P.R. Griffiths), John Wiley & Sons, Ltd., Chichester.

35 Korkmaz, F., Köster, S., Yildiz, Ö., and Mäntele, W. (2008) The role of lipids for the functional integrity of porin: an FTIR study using lipid and protein reporter groups. *Biochemistry*, **47**, 12126–12134.

36 Tyagi, G., Jangir, D.K., Singh, P., and Mehrotra, R. (2010) DNA interaction studies of an anticancer plant alkaloid, vincristine, using Fourier transform infrared spectroscopy. *DNA Cell Biol.*, **29**, 693–699.

37 Tyagi, G., Pradhan, S., Srivastava, T., and Mehrotra, R. (2014) Nucleic acid binding properties of allicin: spectroscopic analysis and estimation of anti-tumor potential. *Biochim. Biophys. Acta*, **1840**, 350–356.

38 Bourassa, P. and Tajmir-Riahi, H.A. (2015) Folic acid binds DNA and RNA at different locations. *Int. J. Biol. Macromol.*, **74**, 337–342.

39 Wehrli, F.W. and Wirthlin, T. (1976) *Interpretation of Carbon-13 NMR Spectra*, Heyden & Son Ltd., London.

40 Zerbe, O. and Jurt, S. (2014) *Applied NMR Spectroscopy for Chemists and Life Scientists*, Wiley-VCH Verlag GmbH & Co. KGaA, Weinheim.

41 Günther, H. (2013) *NMR Spectroscopy: Basic Principles, Concepts and Applications in Chemistry*, Wiley-VCH Verlag GmbH, Weinheim.

42 Che, M. and Vedrine, J.C. (eds) (2012) *Characterization of Solid Materials and Heterogeneous Catalysts: From Structure to Surface Reactivity*, Wiley-VCH Verlag GmbH & Co. KGaA, Weinheim.

43 Laws, D.D., Bitter, H.-M.L., and Jerschow, A. (2002) Solid-state NMR spectroscopic methods in chemistry. *Angew. Chem. Int. Ed.*, **41**, 3096–3129.

44 Jackowski, K. and Jaszuński, M. (eds) (2016) *Gas Phase NMR*, Royal Society of Chemistry, London.

45 Lambert, J.B. and Mazzola, E.P. (2004) *Nuclear Magnetic Resonance Spectroscopy: An Introduction to Principles, Applications, and Experimental Methods*, Pearson Education, Upper Saddle River, NJ.

46 Ablett, S. (1992) Overview of NMR applications in food science. *Trends Food Sci. Technol.*, **3**, 246–250.

47 Preston, C.M. (1996) Applications of NMR to soil organic matter analysis: history and prospects. *Soil Sci.*, **161**(3), 144–166.

48 Marcone, M.F., Wang, S., Albabish, W., Nie, S., Somnarain, D., and Hill, A. (2013) Diverse food-based applications of nuclear magnetic resonance (NMR) technology. *Food Res. Int.*, **51**(2), 729–747.

49 Demco, D.E. and Blümich, B. (2001) NMR imaging of materials. *Curr. Opin. Solid State Mater. Sci.*, **5**(2-3), 195–202.

50 Diercks, T., Coles, M., and Kessler, H. (2001) Applications of NMR in drug discovery. *Curr. Opin. Chem. Biol.*, **5**, 285–291.

51 Goldstein, J., Newbury, D., Joy, D., Lyman, C., Echlin, P., Lifshin, E., Sawyer, L., and Michael, J. (2012) *Scanning Electron Microscopy and X-Ray Microanalysis: a Text for Biologists, Materials Scientists, and Geologists*, Springer Science & Business Media.

52 Kimseng, K. and Meissel, M. (2001) *Short Overview about the ESEM: The Environmental Scanning Electron Microscope*, Produced by CALCE Electronic Products and Systems Centre, University of Maryland, Maryland.

53 Yang, D.S., Mohammed, O.F., and Zewail, A.H. (2013) Environmental scanning ultrafast electron microscopy: structural dynamics of solvation at interfaces. *Angew. Chem. Int. Ed.*, **52**(10), 2897–2901.

54 Microscope Master http://www.microscopemaster.com/transmission-electron-microscope.html (accessed 10 February 2016).

55 Kumar, C.S. (2013) *Transmission Electron Microscopy Characterization of Nanomaterials*, Springer Science & Business Media.

56 Williams, D.B. and Carter, C.B. (1996) *The Transmission Electron Microscope*, Springer, New York.

57 FEI https://www.fei.com/documents/introduction-to-microscopy-document (accessed 10 February 2016).

58 The University of Iowa http://cmrf.research.uiowa.edu/transmission-electron-microscopy (accessed 10 February 2016).

59 Yin, H., Wang, C., Zhu, H., Overbury, S.H., Sun, S., and Dai, S. (2008) Colloidal deposition synthesis of supported gold nanocatalysts based on Au–Fe 3 O 4 dumbbell nanoparticles. *Chem. Commun.*, **36**, 4357–4359.

60 Li, X.J., He, L.L., Li, Y.S., Yang, Q., and Hirose, A. (2015) Characterization of boron doped diamond-like carbon film by HRTEM. *Appl. Surf. Sci.*, **357**, 2141–2146.

61 Akamine, H., van den Bos, K.H.W., Gauquelin, N., Farjami, S., Van Aert, S., Schryvers, D., and Nishida, M. (2015) Determination of the atomic width of an APB in ordered CoPt using quantified HAADF-STEM. *J. Alloys Compd.*, **644**, 570–574.

62 Hollander, A. and Danino, D. (2015) Cochleate characterization by cryogenic electron microscopymethods: Cryo-TEM and Cryo-SEM. *Colloids Surf., A*, **483**, 187–192.

63 http://webmediinfo.blogspot.com.tr/2012/02/microtome.html (accessed 30 May 2016).

64 Leng, Y. (2013) *Materials Characterization: Introduction to Microscopic and Spectroscopic Methods*, 2nd edn, John Wiley & Sons, Ltd.

65 Binnig, G., Rohrer, H., Gerber, C., and Weibel, E. (1982) Surface studies by scanning tunneling microscopy. *Phys. Rev. Lett.*, **49**(1), 57.

66 Nobelprize.org http://www.nobelprize.org/nobel-prizes/physics/laureates/1986/press.html (accessed 5 January 2016).

67 Binnig, G., Quate, C.F., and Gerber, C. (1986) Atomic force microscope. *Phys. Rev. Lett.*, **56**(9), 930.

68 Roy, R. and Desai, J.P. (2014) Determination of mechanical properties of spatially heterogeneous breast tissue specimens using contact mode atomic force microscopy (AFM). *Ann. Biomed. Eng.*, **42**(9), 1806–1822.

69 Guillermet, O., Gauthier, S., Joachim, C., De Mendoza, P., Lauterbach, T., and Echavarren, A. (2011) STM and AFM high resolution intramolecular imaging of a single decastarphene molecule. *Chem. Phys. Lett.*, **511**(4), 482–485.

70 Turkan, U. and Guden, M. (2010) The effect of surface treatment on CaP deposition of Ti6Al4V open cell foams in SBF solution. *Ceram. Int.*, **36**(6), 1805–1816.

71 Campen, S., Green, J.H., Lamb, G.D., and Spikes, H.A. (2015) *In situ* study of model organic friction modifiers using liquid cell AFM: self-assembly of octadecylamine. *Tribol. Lett.*, **58**(3), 1–15.

72 Shin, H.J., Kim, S.H., Yang, H., and Kuk, Y. (2014) Modified gap states in Fe/MgO/SrTiO 3 interfaces studied with scanning tunneling microscopy. *Curr. Appl. Phys.*, **14**(12), 1692–1695.

73 Varghese, B., Piramanayagam, S.N., Lee, W.K., and Tan, H.K. (2014) Noise characterization of perpendicular recording media by cluster size measurements. *IEEE Trans. Magn.*, **50**(5), 1–6.

74 Kazakova, O., Panchal, V., and Burnett, T.L. (2013) Epitaxial graphene and graphene–based devices studied by electrical scanning probe microscopy. *Crystals*, **3**(1), 191–233.

75 Pruneanu, S., Olenic, L., Al-Said, S.A.F., Borodi, G., Houlton, A., and Horrocks, B.R. (2010) Template and template-free preparation of one-dimensional metallic nanostructures. *J. Mater. Sci.*, **45**(12), 3151–3159.

76 Taran, E., Kanda, Y., Vakarelski, I.U., and Higashitani, K. (2007) Nonlinear friction characteristics between silica surfaces in high pH solution. *J. Colloid Interface Sci.*, **307**(2), 425–432.

77 Enax, J., Janus, A.M., Raabe, D., Epple, M., and Fabritius, H.O. (2014) Ultrastructural organization and micromechanical properties of shark tooth enameloid. *Acta Biomater.*, **10**(9), 3959–3968.

78 Tekaya, A., Benameur, T., Labdi, S., and Aubert, P. (2013) Effect of Ti/TiN multilayer protective nanocoatings on Zr-based metallic glasses mechanical performance. *Thin Solid Films*, **539**, 215–221.

79 Cassie, A.B.D. and Baxter, S. (1944) Wettability of porous surfaces. *Trans. Faraday Soc.*, **40**, 546–551.

80 Wenzel, R.N. (1936) Resistance of solid surfaces to wetting by water. *Ind. Eng. Chem.*, **28**(8), 988–994.

81 Wenzel, R.N. (1949) Surface roughness and contact angle. *J. Phys. Chem.*, **53**(9), 1466–1467.

82 Fox, H.W. and Zisman, W.A. (1950) The spreading of liquids on low energy surfaces. *J. Colloid Sci.*, **5**, 514–531.

83 Owens, D.K. and Wendt, R.C. (1969) Estimation of the surface free energy of polymers. *J. Appl. Polym. Sci.*, **13**(8), 1741–1747.

84 Janczuk, B. and Bialopiotrowicz, T. (1989) Surface free-energy components of liquids and low energy solids and contact angles. *J. Colloid Interface Sci.*, **127**, 189–204.

85 Washburn, E.W. (1921) The dynamics of capillary flow. *Phys. Rev.*, **17**, 273–283.

86 Van Oss, C.J., Giese, R.F., Li, Z., Murphy, K., Norris, J., Chaudhury, M.K., and Good, R.J. (1992) Determination of contact angles and pore sizes of porous media by column and thin layer wicking. *J. Adhes. Sci. Technol.*, **6** (4), 413–428.

87 Sing, K.S.W., Everett, D.H., Haul, R.A.W., Moscou, L., Pierotti, R.A., Rouquerol, J., and Siemieniewska, T. (1985) Physical and biophysical chemistry division commission on colloid and surface chemistry including catalysis. *Pure Appl. Chem.*, **57**(4), 603–619.

88 Lowell, S., Shields, J.E., Thomas, M.A., and Thommes, M. (2012) *Characterization of Porous Solids and Powders: Surface Area, Pore Size and Density*, vol. **16**, Springer Science & Business Media.

89 Hill, T.L. (1949) Physical adsorption and the free volume model for liquids. *J. Chem. Phys.*, **17**(6), 590.

90 Langmuir, I. (1918) The adsorption of gases on plane surfaces of glass, mica and platinum. *J. Am. Chem. Soc.*, **40**(9), 1361–1403.

91 Brunauer, S., Emmett, P.H., and Teller, E. (1938) Adsorption of gases in multimolecular layers. *J. Am. Chem. Soc.*, **60**(2), 309–319.

92 Carmody, O., Frost, R., Xi, Y., and Kokot, S. (2007) Surface characterisation of selected sorbent materials for common hydrocarbon fuels. *Surf. Sci.*, **601**(9), 2066–2076.

93 Smith, P.R.D., Auston, H., and Nuss, M.C. (1988) Subpicosecond photoconducting dipole antennas. *IEEE J. Quantum Electron.*, **24**, 255–260.

94 Piao, Z., Tani, M., and Sakai, K. (2000) Carrier dynamics and terahertz radiation in photoconductive antennas. *Jpn. J. Appl. Phys.*, **39**, 96–100.

95 Dragoman, D. (2004) Terahertz fields and applications. *Prog. Quantum Electron.*, **28**, 1–66.

96 Nahata, A., Weling, A.S., and Heinz, T.F. (1996) A wideband coherent terahertz spectroscopy system using optical rectification and electro-optic sampling. *Appl. Phys. Lett.*, **69**, 2321–2323.

97 Schneider, A., Neis, M., Stillhart, M., Ruiz, B., Khan, R.U.A., and Günter, P. (2006) Generation of terahertz pulses through optical rectification in

organic DAST crystals: theory and experiment. *J. Opt. Soc. Am. B*, **23**, 1822–1835.

98 Ding, Y.J. and Shi, W. (2006) Efficient THz generation and frequency upconversion in GaP crystals. *Solid-State Electron.*, **50**, 1128–1136.

99 Yajima, T. and Takeuchi, N. (1970) Far-infrared difference-frequency generation by picosecond laser pulses. *Jpn. J. Appl. Phys.*, **9**, 1361–1371.

100 Tani, M., Herrmann, M., and Sakai, K. (2002) Generation and detection of terahertz pulsed radiation with photoconductive antennas and its application to imaging. *Meas. Sci. Technol.*, **13**, 1739–1745.

101 Wu, Q. and Zhang, X.-C. (1996) Ultrafast electro-optic field sensors. *Appl. Phys. Lett.*, **68**, 1604–1606.

102 Cai, Y., Brener, I., Lopata, J., Wynn, J., Pfeiffer, L., Stark, J.B., Wu, Q., Zhang, X.-C., and Federici, J.F. (1998) Coherent terahertz radiation detection: direct comparison between free-space electro-optic sampling and antenna detection. *Appl. Phys. Lett.*, **73**, 444–446.

103 Han, P.Y., Tani, M., Usami, M., Kono, S., Kersing, R., and Zhang, X.C. (2001) A direct comparison between terahertz time-domain spectroscopy and far-infrared Fourier transform spectroscopy. *J. Appl. Phys.*, **89**, 2357–2359.

104 Jeon, T.-I. and Grischkowsky, D. (1998) Characterization of optically dense, doped semiconductors by reflection THz time domain spectroscopy. *Appl. Phys. Lett.*, **72**, 3032–3034.

105 Nashima, S., Morikawa, O., Takata, K., and Hangyo, M. (2001) Measurement of optical properties of highly doped silicon by terahertz time domain reflection spectroscopy. *Appl. Phys. Lett.*, **79**, 3923–3925.

106 Kužel, P. and Petzelt, J. (2000) Time-resolved terahertz transmission spectroscopy of dielectrics. *Ferroelectrics*, **239**, 949–956.

107 Nishizawa, S., Sakai, K., Hangyo, M., Nagashima, T., Takeda, M.W., Tominaga, K., Oka, A., Tanaka, K., and Morikawa, O. (2005) in *Terahertz Optoelectronics* (ed. K. Sakai), Springer, Berlin-Heidelberg, Germany, pp. 203–271.

108 Naftaly, M. and Miles, R.E. (2007) Terahertz time-domain spectroscopy for material characterization. *Proc. IEEE*, **95**(8), 1658–1665.

109 Wallace, V.P., Taday, P.F., Fitzgerald, A.J., Woodward, R.M., Cluff, J., Pye, R.J., and Arnone, D.D. (2004) Terahertz pulsed imaging and spectroscopy for biomedical and pharmaceutical applications. *Faraday Discuss.*, **126**, 255–263.

110 Duling, I. and Zimdars, D. (2009) Terahertz imaging: revealing hidden defects. *Nat. Photonics*, **3**, 630–632.

111 Shen, Y., Lo, T., Taday, P.F., Cole, B.E., Tribe, W.R., and Kemp, M.C. (2005) Detection and identification of explosives using terahertz pulsed spectroscopic imaging. *Appl. Phys. Lett.*, **86**, 241116.

112 Yang, Y., Mandehgar, M., and Grischkowsky, D. (2015) THz-TDS characterization of the digital communication channels of the atmosphere and the enabled applications. *J. Infrared Millimeter Terahertz Waves*, **36**, 97–129.